Arabian Journal for Science and Engineering (2024) 49:14927–14948
https://doi.org/10.1007/s13369-024-08855-4

RESEARCH ARTICLE-MECHANICAL ENGINEERING

Effect of Carbon Nanotube Reinforcement on Creep and Recovery Behavior of Additively Manufactured Polymers: An Experimental and Prediction Study

Kamil Feratoğlu[1] · İlyas İstif[2] · Ömer Yunus Gümüş[3] · Erol Türkeş[1]

Received: 9 October 2023 / Accepted: 8 February 2024 / Published online: 13 March 2024
© The Author(s) 2024

Abstract
In this study, one of the most frequently used polymeric materials in fused deposition modeling (FDM) acrylonitrile butadiene styrene (ABS) is reinforced with different amount of carbon nanotubes (CNTs). Thermogravimetric analysis and differential scanning calorimetry analysis are applied to examine thermal degradation behavior of produced nanocomposite filaments. Specimens are manufactured by fused deposition modeling by using produced nanocomposite filaments. Tensile, creep and viscoelastic-viscoplastic behaviors of FDM-printed nanocomposite samples are investigated by conducting tensile, creep and loading–unloading tests under different strain rates and strain levels. Morphology of 3D printed samples is examined through scanning electron microscopy. Void densities which plays important role in mechanical behavior of additively manufactured samples are determined via ImageJ and CNT reinforcement on void densities are investigated. Data obtained from tests are used in system identification process, and multi-input–single-output model structures are proposed for the prediction of tensile, creep and recovery behaviors of 3D printed nanocomposite materials.

Keywords Fused deposition modeling · Nanocomposite polymers · Creep behavior · Viscoelastic behavior · Identification · Artificial neural network

1 Introduction

Fused deposition modeling (FDM), fused filament fabrication (FFF) or 3D printing has gained popularity over other additive manufacturing techniques due to their low cost and diversity of usable material [1]. In this technique, filament which is heated above its glass transition temperature passes through a nozzle and deposited onto a platform layer by layer [2]. Engineering polymers such as polycarbonate (PC), nylon 12, polylactic acid (PLA) and acrylonitrile butadiene styrene (ABS) are most preferred materials in FDM technology [3–5]. However, 3D printed parts produced with these pure polymers are insufficient for functional use due to their poor mechanical properties [6, 7]. Hence, enhancing the mechanical properties of FDM parts would eliminate the limitations. Many studies focus on improving printing process and optimizing process parameters to overcome these limitations [1–5, 8–14]. Recently, composite filament production for use in 3D printing has been pursued. Adding small amount of fillers to the polymer matrix improve their mechanical properties substantially. For this purpose, carbon-based materials such as graphene [15–18], graphene oxide [19], carbon black [20] and carbon nanotube [21–23] have been extensively used.

In many industrial applications, long-term durability and reliability under applied loads are one of the fundamental

✉ İlyas İstif
istif@yildiz.edu.tr

Kamil Feratoğlu
kamilferatoglu@klu.edu.tr

Ömer Yunus Gümüş
omer.gumus@btu.edu.tr

Erol Türkeş
erol.turkes@klu.edu.tr

1 Department of Mechanical Engineering, Faculty of Engineering, Kirklareli University, Kayali Campus, 39020 Merkez, Kirklareli, Turkey

2 Department of Mechanical Engineering, Faculty of Mechanical Engineering, Yildiz Technical University, Yildiz Campus, 34349 Beşiktaş, Istanbul, Turkey

3 Department of Polymer Materials Engineering, Faculty of Engineering and Natural Sciences, Bursa Technical University, Mimar Sinan Campus, 16310 Yildirim, Bursa, Turkey

quality assurances. Dimensional stability issues could occur due to creep deformation, and it could affect service life and reliability of 3D printed parts. Therefore, inadequate creep resistance in FDM parts indicates nonfunctionality for long-term loading conditions [24]. Comprehensive studies which examine the creep behavior of 3D printed materials has been conducted by the researchers. However, mostly pure polymers are subjected in these studies. Zhang et al. [25] examine the tensile, creep and fatigue behavior of 3D printed ABS parts. Niaza et al. [26] conduct studies on FDM-printed PLA scaffolds to examine creep and impact properties. In addition to these, polymeric materials show strain rate-dependent mechanical behaviors. Hence, beside the tests such as tensile, compression, bending and creep, it is necessary to investigate viscoelastic and viscoplastic behaviors. Literature studies which investigate strain rate-dependent behavior, loading–unloading behavior and resistance to permanent deformation of FDM-printed nanocomposites are very limited. Istif et al. [27] conduct loading–unloading tests at different strain rates to study viscoelastic–viscoplastic properties of PLA samples manufactured by FDM. Prashanta et al. [6] reinforce PLA matrix with different fillers and investigate its viscoelastic properties with dynamic mechanical analysis (DMA). Yin et al. [28] study the viscoelastic deformation of 3D printed PC, ABS and PC/ABS blends. Mohamed et al. [29] examine the time-dependent mechanical properties of printed PC-ABS parts by conducting DMA tests at different frequencies. Dakshinamurthy et al. [30] manufacture ABS parts with different process parameters and analyze their viscoelastic properties. FDM-printed parts have air gaps within their internal structure due to nature of layer-by-layer manufacturing technique, and this gives rise to nonlinear mechanical behavior. Accordingly, numerical modeling techniques are insufficient to predict mechanical behaviors of 3D printed parts. Recently, artificial neural network (ANN) has been incorporated as a prediction tool in estimation of mechanical behaviors of additively manufactured materials. ANN and fuzzy logic-based prediction methods show excellent performance in modeling of complex mechanisms which have nonlinear relations [31]. Limited number of studies in the literature have dealt with optimizing the FDM process parameters by using ANN methods. Peng et al. [32] optimize the FDM process parameters by using response surface methodology (RSM) and ANN techniques to increase dimensional accuracy of printed samples. Sood et al. [33] investigate the influence of different FDM process parameters on compressive strength of 3D printed samples by using ANN method.

In this study, FDM-printed ABS plastic which has gained importance in various industries such as automotive, aerospace, medical and consumer goods is used as matrix material, and various amounts of MWCNTs are added to ABS as reinforcement material. The CNTs have been frequently employed to design a high damping composite with significant creep and recovery behaviors [34, 35]. Due to their excellent mechanical properties, high flexibility and low density CNTs are the most preferred among the other nanofillers in manufacturing of polymer composites [36–39]. Achieving a homogeneous dispersion in polymer matrix is relatively difficult for CNTs due their strong van der Waals bonds [40–44]. Nevertheless, produced nanocomposites shows excellent performance if homogeneous dispersion and compatibility of CNTs with the matrix is provided at a satisfactory level [45]. Structural defects of CNTs provoke the nucleation sites which lead to increasing interaction and triggering stronger bonds [45–48]. Cha et al. [49] add CNT fillers to epoxy resins to strengthen its mechanical properties. Results indicate that the elastic modulus and tensile strength of the produced nanocomposites are increased by 64% and 22%, respectively, with the 2 wt% CNT addition. Pan et al. [50] report that epoxy's loss factor is escalated by 41.1% owing to 0.4 wt% CNTs. Xu et al. [34] produce epoxy resin based composites with high stiffness and high damping ratio. Epoxy resins are used as matrix material. While dangling chains and the soft curing agent increase the damping, stiffness of the produced material is decreased. To prevent this negative effect on modulus, MWCNTs are used as reinforcement material.

Objective of this study is to enhance creep, rate-dependent and recovery behaviors of 3D printed ABS materials by means of CNT reinforcement. Besides, models with multi-input and single-output structures are developed by using system identification to predict mechanical behaviors of FDM-printed nanocomposites. Time, rate and recovery behaviors of 3D printed materials are limited in the literature. To author knowledge, prediction of abovementioned behaviors of 3D printed parts is not elaborated extensively. For this purpose, ABS-CNT nanocomposites are produced in filament form to use in FDM process. Thermal degradation behavior of produced filaments are investigated by conducted differential scanning calorimetry (DSC) and thermogravimetric analyses (TGA). Filaments are used to manufacture parts in a 3D printer. FDM-printed samples' time- and strain rate-dependent behaviors are examined by conducting tensile, creep and loading–unloading tests. Porous structure which has great influence on the mechanical strength of 3D printed materials are examined through scanning electron microscopy (SEM) and effect of CNT reinforcement on void density is investigated.

In a preceding investigation, we formulate a nonlinear model employing the nonlinear ARX structure, incorporating a sigmoid network with a single hidden layer. This model is designed to replicate the wear characteristics of the brake lining material [31]. In a separate study, we improve the NARX model by introducing a multiple-input–single-output (MISO) structure. In this configuration, wear rate serves as

the output variable, while input variables include the coefficient of friction (COF), ambient temperature, and the quantity of nanofiller [51]. In our present study, model structure are adapted to mechanical test processes. Data preparation and normalization process has been applied to mechanical test data. Provided data from the conducted tensile, creep and loading–unloading tests are used to establish multi-input–single-output (MISO) ANN-based nonlinear autoregressive exogenous (NARX) model structures for each test. Beside that, transfer function and process model structures are also presented for the comparison with the NARX models. The originality of the article stems from the thorough examination of the mechanical properties including creep, rate-dependent and recovery behavior of 3D printed ABS material reinforced with CNT, using a combination of experimental testing and computational modeling. Additionally, the utilization of a MISO model structure and contributes to the novelty of the research.

2 Materials and Methods

2.1 Filament Production

Matrix material ABS is supplied in granular form. According to technical data provided by the manufacturer, the density and the volumetric melting rate are 1.04 g/cm3 and 14 cm3/10 min (@220 °C/10 kg), respectively. Prior to filament production ABS granules are dehumidified for 2 h at 70 °C in drying oven. Functionalized (–COOH) multiwall carbon nanotubes are purchased from Nanografi Nano Technology. CNTs have length of 5–10 μm, diameter of 10–20 nm and the purity is 96% according to data sheet. To achieve adequate adhesion between CNT and the polymer matrix, ABS in granule form is pulverized and pulverized ABS is blended with 2 wt%, 4 wt% and 6 wt% CNTs. Then, ABS-CNT blends are fed into the twin screw extruder ($D = 18$ mm; $L/D = 40$, Polmak) for melt blending process. Process is conducted at varying temperatures of 220–240 °C and varying screw speed of 10–20 rpm which are determined by taking into account the amount of CNTs in the polymer matrix. After the melt blending process, semi-finished composite product are pelletized in granulization device. Prior to feeding into filament production line, pellets are dehumidified at 70 °C for 4 h in a furnace. Final product as nanocomposite filament is obtained from single screw extruder with a diameter of ~ 1.75 mm. Single screw extruder contains feeding unit, three heating zone, water tank for cooling process and winding unit for the filament. Heating zone temperatures, screw and traction servo speed for the filament production line are shown in Fig. 1.

All stages of nanocomposite filament production are shown in Fig. 2. Homogeneous dispersion of nanoparticles in polymer matrix is crucial for the better mechanical properties of 3D printed parts as mentioned before. Unlike the other approaches, prior to melt blending process polymer granules are pulverized for the better adhesion between polymer matrix and nanoparticles.

2.2 Thermal Degradation Behavior

10 mg of samples taken from produced filaments are subjected to thermogravimetric analysis (TGA) to determine if the amount of nanoparticles in the polymer matrix is coincide with the nominal reinforcement values. TA/SDT650 gravimetric analysis device is used, and the analysis is conducted between temperature of 30 °C and 900 °C at 10 °C/ min heating rate.

It is essential to determine bed temperature for the better adhesion between platform and 3D printed part. Literature studies indicate that selecting bed temperature close to the glass transition temperature (T_g) ensures the best possible results [52]. Differential scanning calorimetry analyses are conducted by using TA Discovery DSC 250 device to determine T_g values of manufactured filaments. Tests are carried out on 10 mg samples with heating and cooling cycles under varying temperatures between 30 and 300 °C.

2.3 FDM-Printed Specimens

During 3D printing of nanocomposites most encountered problem is nozzle clogging. Escalating brittleness due to increasing amount of nanoparticles or agglomeration of nanoparticles in polymer matrix could cause the problem. In this study, 0.4 mm nozzles are used primarily during FDM process. Although there is no problem encountered during the printing of pure ABS, clogging occurs during the printing of CNT-reinforced ABS materials. Therefore, 0.8-mm nozzle is chosen for the production. Specimens for tensile, creep and loading–unloading tests are manufactured in accordance with ASTM D638 -14 (Standard Test Method for Tensile Properties of Plastics-Type IV) and printing is performed with a Creality 3D Cr 6 Se printer.

Nozzle temperatures for pure ABS, ABS—2 wt% CNT, ABS—4 wt% CNT and ABS—6 wt% CNT are selected as 240 °C, 250 °C, 250 °C and 255 °C, respectively. 110 °C is preferred for the bed temperature which is close to glass transition temperature of ABS-CNT nanocomposites (~ 109 °C). Prior to 3D printing process, prepared test specimen files in SOLIDWORKS software according to abovementioned standards are sliced using Ultimaker Cura 4.10.0 software. To observe the effect of CNT reinforcement on deposited filament adhesion, line ($[+45°, -45°]$) and concentric ($[0, 90°]$) infill types (Fig. 3) which have adequate adhesions between neighboring fibers are incorporated in FDM process. Printed specimens are shown in Fig. 4.

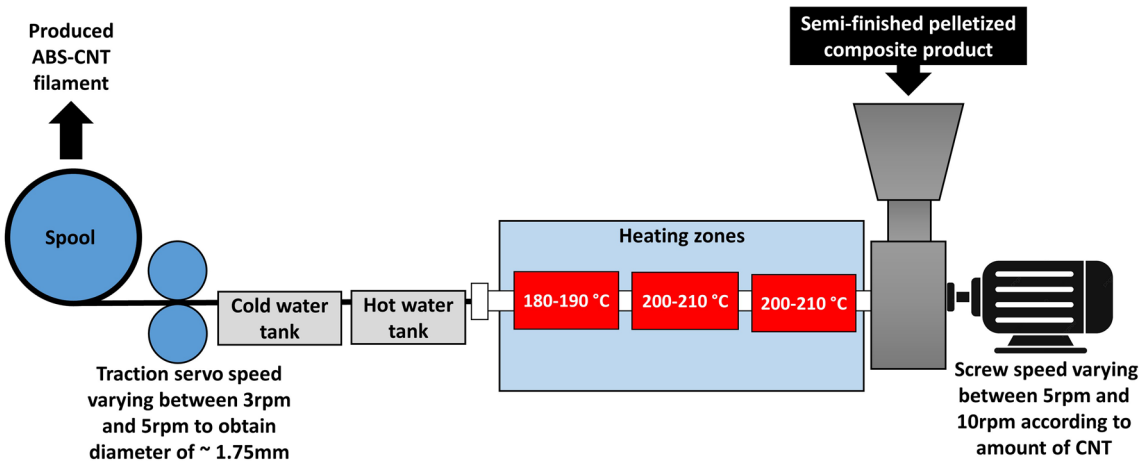


Fig. 1 Filament production line and parameters (single-screw extruder)

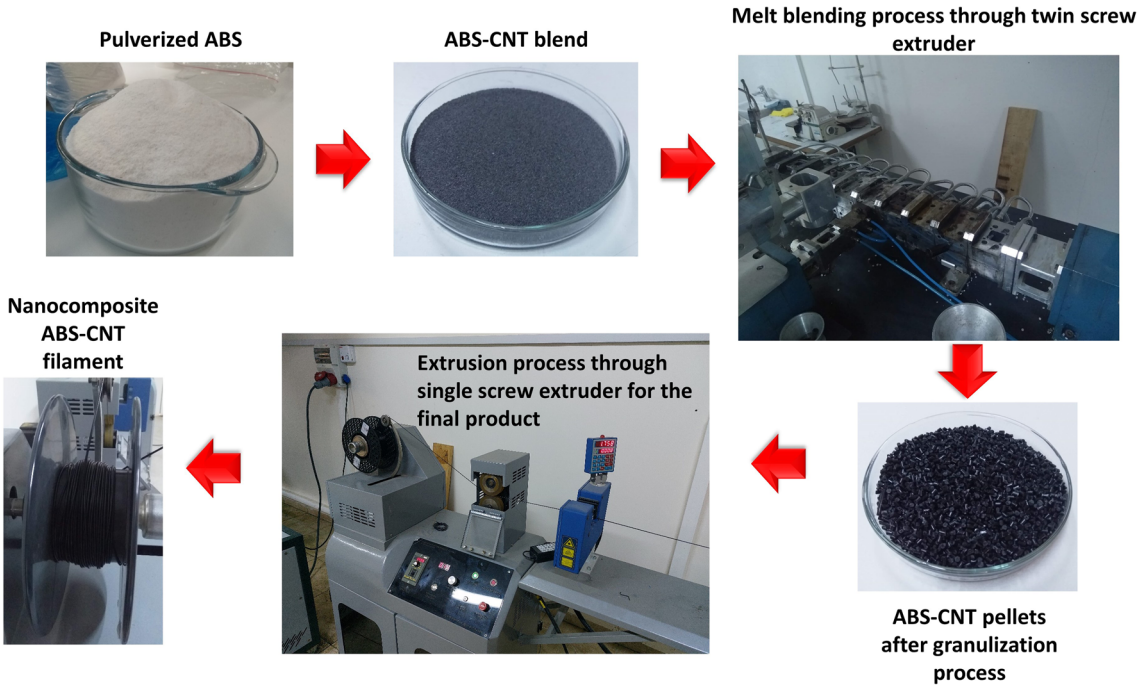


Fig. 2 Nanocomposite filament production process

2.4 Determining Void Area Densities

Due to layer-by-layer manufacturing technique, FDM-printed parts have voids in their internal structure, and these voids have a significant effect on mechanical behavior. Therefore, voids and their effects must be incorporated into the model structure to predict behavior accurately. For this purpose, section area perpendicular to tensile direction is picked for each specimen. Two-dimensional section areas and voids contained within them are examined with scanning electron microscopy (SEM). Provided SEM images are studied in ImageJ software to determine void density for each specimen. Samples with concentric infill pattern is used for void density determination. Because, their fiber alignment is parallel to tensile direction and determining the 2D void density in the cross section of specimen would be equivalent to determining the void density for entire specimen volume.

2.5 Mechanical Tests

2.5.1 Quasi-Static Tensile and Cyclic Tests

Tensile, creep and loading–unloading tests of CNT-reinforced FDM-printed polymers are conducted on SHIMADZU universal testing equipment with 10 kN load cell (Fig. 5). Tensile test specimens printed in accordance with

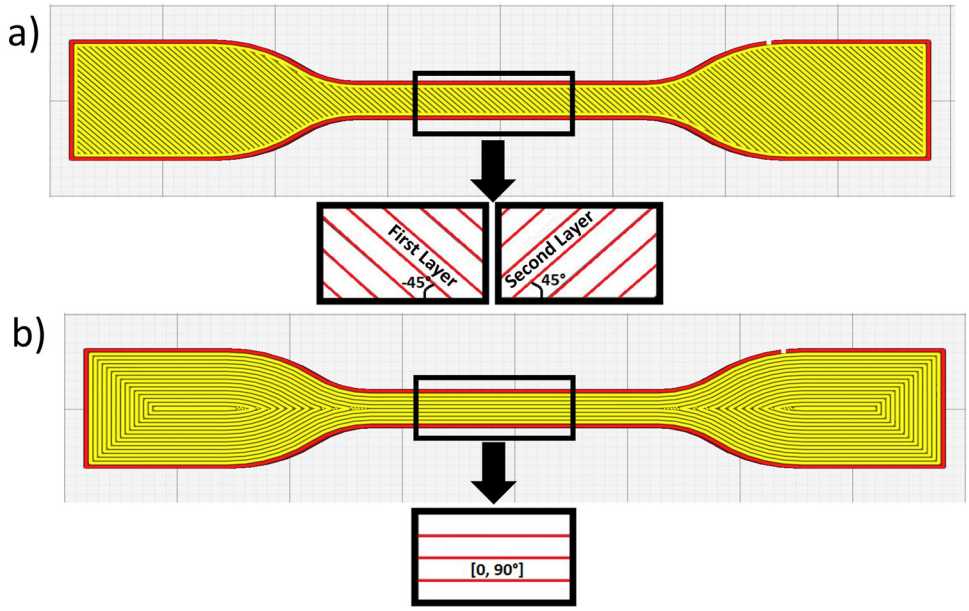


Fig. 3 Infill types; **a** Line (+ 45°, − 45°), **b** Concentric (0,90°)



Fig. 4 FDM-printed specimens

ASTM D638-14 standards. Tensile and loading–unloading tests are performed at 1E-3 (1.5 mm/min) and 1E-4 (0.15 mm/min) strain rates to examine strain rate-dependent behaviors of the printed specimens. For each condition, four samples are used and their averages are taken.

Quasi-static loading–unloading tests are conducted under elastic (viscoelastic) region, and corresponding strain levels are selected as %3 and %5. Along with the hysteretic behaviors, strain rate-dependent behaviors of are also examined with quasi-static loading–unloading tests. Data obtained from loading–unloading tests are used to examine recovery and viscoelastic behaviors of 3D printed CNT-reinforced polymers. Hysteresis cycles and area under these curves are calculated with integration method by using Origin Pro 2021 software (Fig. 6).

2.5.2 Creep Tests

Creep tests are performed at room temperature according to ASTM D2990-17 standards. Prior to creep tests, proper stress level is specified to conduct creep under viscoelastic deformation regime. Tests are performed under 16.25 MPa stress level for 2.78 h. Strain data are recorded as a function of time. Each tests are carried out three times to obtain reliable results. Creep test results are presented via creep compliance-time diagrams. Creep compliance could be defined as the strain response of the component under constant applied stress.

$$J(t) = \frac{\varepsilon(t)}{\sigma} \tag{1}$$



Fig. 5 Tensile testing equipment (SHIMADZU-AGS-X)

In cases where no plastic deformation occurs, isothermal creep compliance consists of two parts: instantaneous elastic compliance (J_{el}) and time-dependent viscoelastic creep compliance (J_{ve}).

$$J_{total}(t) = J_{el} + J_{ve}(t) \tag{2}$$

2.6 Identification Procedure and Modeling

System identification is a technique which is employed for building model structure for dynamic systems. Mathematical models of dynamic systems could be built using input and output data by incorporating statistical methods. Analytical methods are inefficient to construct models for simulating dynamic systems which have nonlinear relations between input and output variables. These nonlinear relations could be predicted efficiently by using smart computing techniques which utilize experimental input–output data [53]. Artificial neural network (ANN) models shows better performance in prediction of dynamic systems comparing to conventional linear system identification methods such as autoregressive moving average model (ARMAX) and Box-Jenkins [54]. ANN-based nonlinear autoregressive with exogenous network (NARX) structures shows excellent performance on

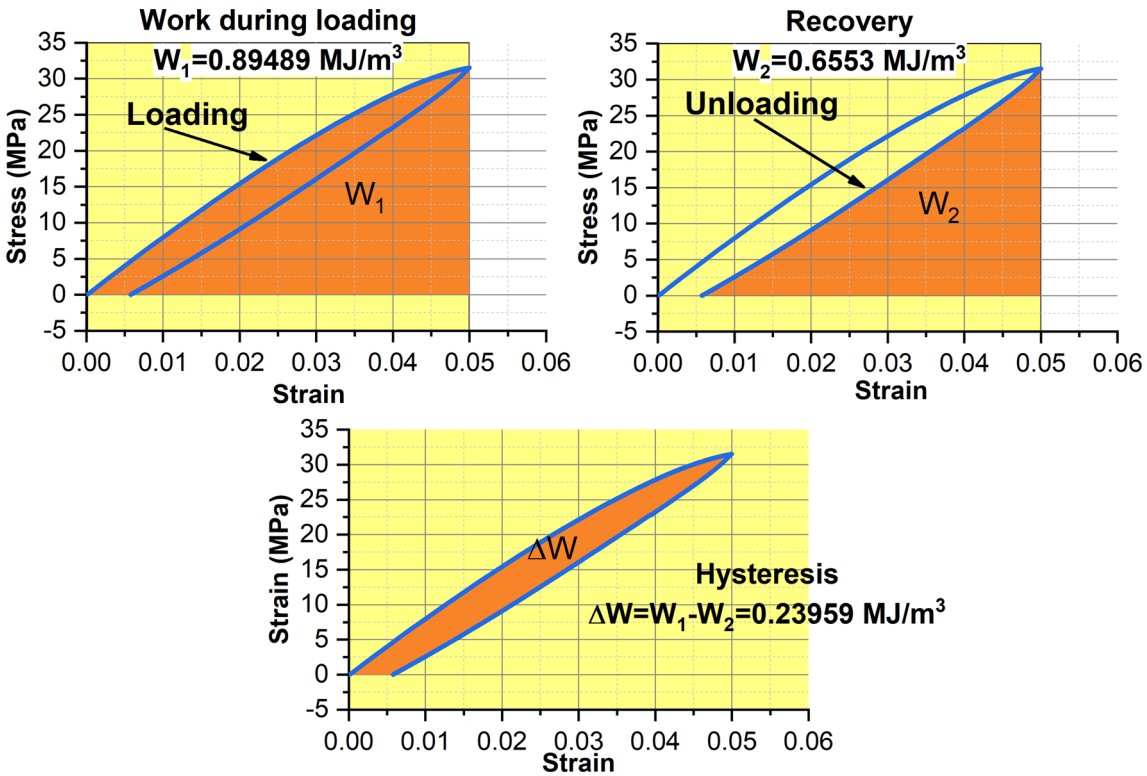


Fig. 6 Determination of elastic recovery and hysteresis

predicting dynamic systems which have sequential datasets. Rapid convergence and ability to model systems with long-term dependencies are the primary benefits of NARX [55].

In our previous study, nonlinear model has been developed by using nonlinear ARX structure with sigmoid network which has one hidden layer to simulate the wear behavior of the brake lining material [31]. In another work, we have improved NARX model and present multiple-input–single-output (MISO) structure. While wear rate is taken as output variable, coefficient of friction (COF), ambient temperature and amount of nanofiller are taken as input variables [51]. In this study, model structure are adapted to mechanical test processes. Data preparation and normalization process have been applied to mechanical test data. Conducted mechanical test processes are assumed as complex nonlinear system, and multi-input–single-output model structures are presented by implementing system identification procedure using MATLAB software. In tensile test and cyclic test processes, while strain data are taken as output variable, void density areas which are determined by processing SEM images via ImageJ, strain rates and applied stress are taken as input variables. In creep test process, while strain data are taken as output variables, void density areas, time (s) and wt% CNT are taken as input variables. Mechanical test data of specimens with concentric infill pattern are used in identification procedure. During the 3D printing process of specimens with concentric infill pattern, the filament which is extruded onto the build platform has the same direction with the tensile test axis, and this direction is uniform along the length of the specimen. Therefore, determining the void area densities are relatively easier than the specimens with line infill pattern.

2.6.1 Data Preparation and Normalization

Prior to including in the model, normalization process is applied to data. Since input variables have different units and magnitudes, data normalization increases the reliability of parameter estimation process in ANN applications. The obtained data from the experiments are converted into a sequential time series. While input variables at a certain time (t_k) are symbolized by the vector ${uj_{t_k}}^i$ for i-th experiment and j-th input, output variables are symbolized by the vector ${yj_{t_k}}^i$. Data matrices having dimensions specific to each experiment and consist of input and output variable vectors are built.

$$x^i = \begin{bmatrix} {u1_{t_1}}^i & \dots & {u1_{t_k}}^i & \dots & {u1_{t_{n_i}}}^i \\ {u2_{t_1}}^i & \dots & {u2_{t_k}}^i & \dots & {u2_{t_{n_i}}}^i \\ {u3_{t_1}}^i & \dots & {u3_{t_k}}^i & \dots & {u3_{t_{n_i}}}^i \\ {y_{t_1}}^i & \dots & {y_{t_k}}^i & \dots & {y_{t_{n_i}}}^i \end{bmatrix} \tag{3}$$

Datasets obtained from tests are usually added to model structure as a group. However, incorporating the data in the abovementioned manner could cause inconsistencies in time series. For instance, different strain responses and strain rates lead to different time durations for the tests. Accordingly, amount of data obtained from the tests are different from each other. Therefore, size of the time series would be different for each experimental data. To prevent this, data amount of each test is duplicated based on the experiment with most data by implementing piecewise cubic interpolation using MATLAB. Abovementioned variable datasets are scaled between [0,1].

$$\breve{u}_{t_k} = \frac{u^i_{t_k}}{\overline{u}},\ \overline{u} = \max_{i,t_k} u^i_{t_k} \tag{4}$$

$$\breve{y}_{t_k} = \frac{y^i_{t_k}}{\overline{y}},\ \overline{y} = \max_{i,t_k} y^i_{t_k} \tag{5}$$

2.6.2 Model Structures

Nonlinear autoregressive exogenous model (NARX) is derived from single-input—single-output (SISO) linear exogenous model (ARX) structure (Eq. 7). Notation of the variables are customized for this study and two delayed input—two delayed output variables are added to structure.

$${y_{t_k}}^i = \begin{bmatrix} {u1_{t_k}}^i \\ {u1_{t_{k-1}}}^i \\ {u1_{t_{k-2}}}^i \\ {u2_{t_k}}^i \\ {u2_{t_{k-1}}}^i \\ {u2_{t_{k-2}}}^i \\ {u3_{t_k}}^i \\ {u3_{t_{k-1}}}^i \\ {u3_{t_{k-2}}}^i \\ {y_{t_{k-1}}}^i \\ {y_{t_{k-2}}}^i \end{bmatrix}^T \cdot \begin{bmatrix} b_1 \\ b_2 \\ b_3 \\ b_4 \\ b_5 \\ b_6 \\ b_7 \\ b_8 \\ b_9 \\ a_1 \\ a_2 \end{bmatrix} \tag{6}$$

Delayed input and output variables are symbolized with ${uj_{t_{k-1}}}^i$, ${uj_{t_{k-2}}}^i$ and ${y_{t_{k-1}}}^i$, ${y_{t_{k-2}}}^i$, respectively. Determined parameters for each input and output are symbolized as b_j and a_j, respectively. Output are predicted by using delayed inputs and outputs which are called regressors in ARX model. NARX model has more flexible mapping function [31]. Beside the abovementioned linear function, NARX has a activation function which provide nonlinearity. NARX model structure is defined by Eq. 7.

$$\widehat{y}_{t_{\text{prediction}}} = L\left\{\sum_{i=1}^{N} w_g S\left(\sum_{j=1}^{9} w_{gj} I_j + \sum_{m=1}^{2} w_{gm} O_m\right)\right\} \tag{7}$$

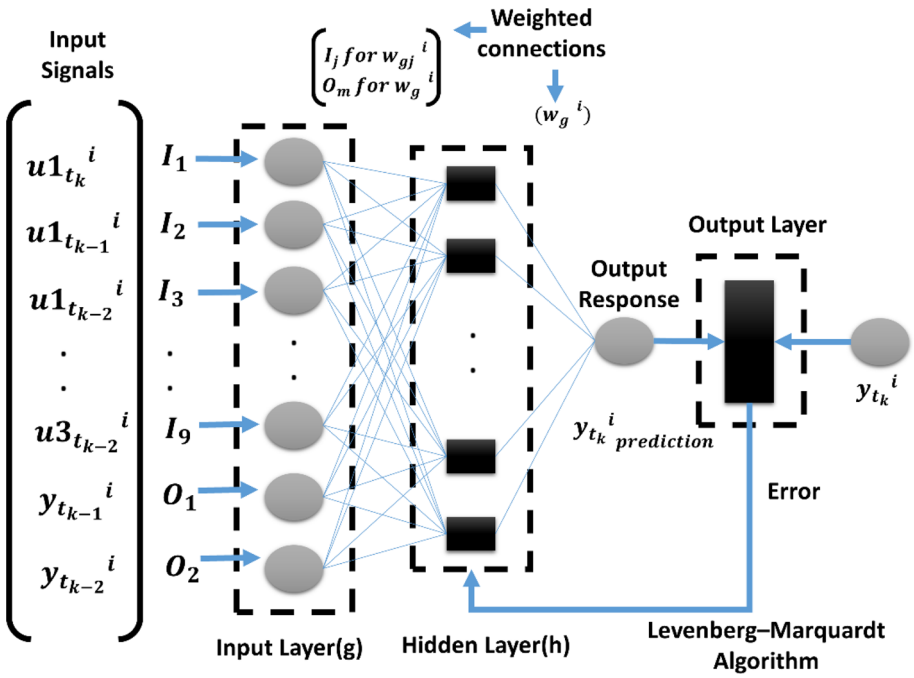


Fig. 7 NARX structure

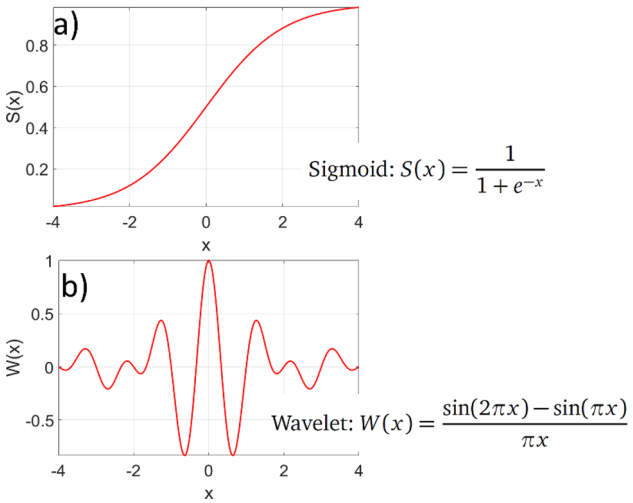


Fig. 8 Activation functions: **a** Sigmoid function, **b** Wavelet function

"L", "S" and "N" represent linear function in ouput layer, activation function in hidden layer and number of neurons in hidden layer, respectively. Input signals are symbolized by "I_j" and "O_m". "w_g", "w_{gj}" and "w_{gm}" represent weights in output and hidden layer. NARX structure is presented in Fig. 7.

Sigmoid and wavelet functions which are shown in Fig. 8 are used as activation functions in the structure. Neurons in hidden layer are transformed into scaled inputs for output layer by activation function. Transfer function (purelin: $g(x) = x$) is used as linear function in output layer. One of the response surface methodology (RSM) methods Levenberg–Marquardt algorithm is incorporated for network optimization.

Transfer function and process models are employed as linear models to compare with NARX model. Levenberg—Marquardt algorithm is used to optimize model parameters. Transfer functions for both models are presented below. In equations, "K_p" is steady-state constant, "T_{p1}" is time constant, "s" is Laplace oprator and "T_d" is time delay.

$$\text{Transfer Function Model}: G(s) = \frac{K_p}{1 + T_{p1}.s} \tag{8}$$

$$\text{Process Model}: G(s) = \frac{K_p}{1 + T_{p1}.s}.e^{-T_d.s} \tag{9}$$

3 Results and Discussion

3.1 Thermal Degradation Behavior

TGA thermograms of ABS-CNT nanocomposite filaments are shown in Fig. 9. Obtained results are presented in Table 1. The onset degradation temperature is defined according to first derivative of weight loss. The residue at 500 °C, 475 °C and 450 °C which are below the fully degradation temperature of ABS-CNT nanocomposites are considered to determine the CNT content based on the equation below:

$$\text{Achieved wt\%CNT} = \text{Residue of composite} - \text{Residue of ABS} \tag{10}$$

Glass transition temperatures (T_g) of produced filaments are determined through DSC thermograms. As a result, CNT addition to ABS matrix has no significant effect on T_g values.

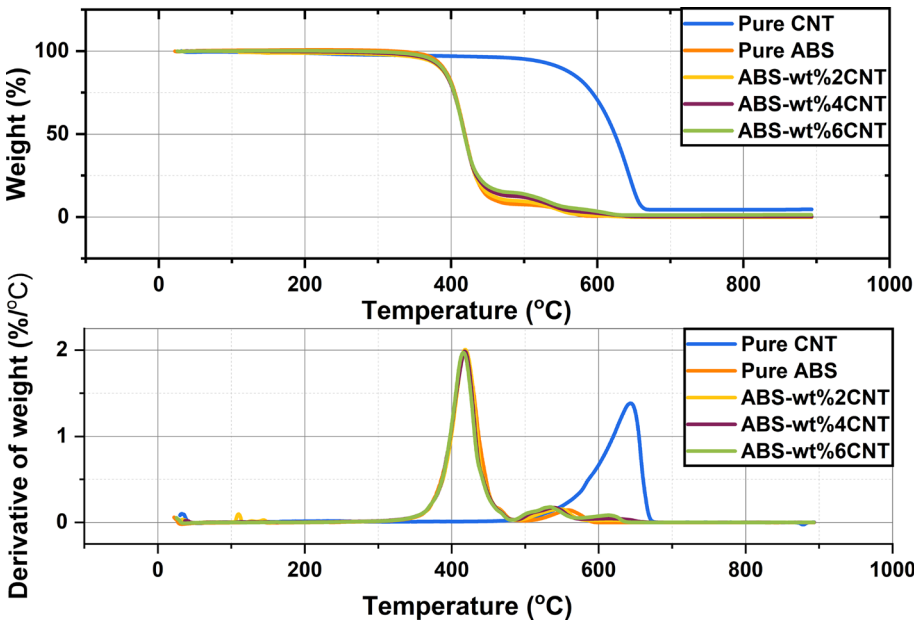


Fig. 9 TGA thermograms for ABS-CNT nanocomposites

Table 1 TGA data in air atmosphere

Material	Residues at 450 °C (%)/Achieved CNT wt%	Residues at 475 °C (%)/Achieved CNT wt%	Residues at 500 °C (%)/Achieved CNT wt%
Pure ABS	12.59	8.2	7.49
ABS-wt%2CNT	14.48 / 1.89	10.3 / 2.1	9.43 / 1.94
ABS-wt%4CNT	16.96 / 4.37	12.95 / 4.75	11.96 / 4.47
ABS-wt%6CNT	18.76 / 6.17	15 / 6.8	13.83 / 6.34

3.2 Determining Void Area Densities via Image J Software

Open-source image processing software ImageJ is used for the determination of void area densities. Areas and lengths on the image could be calculated with user-defined options in the software. Prior to threshold process image is converted into binary format, then images are converted into binary format [56]. After the threshold process, calculations could made with the predetermined scale. Void area densities are determined (Figs. 10, 11).

SEM images of each section of specimens are divided into four parts and each parts' void areas are calculated. Void

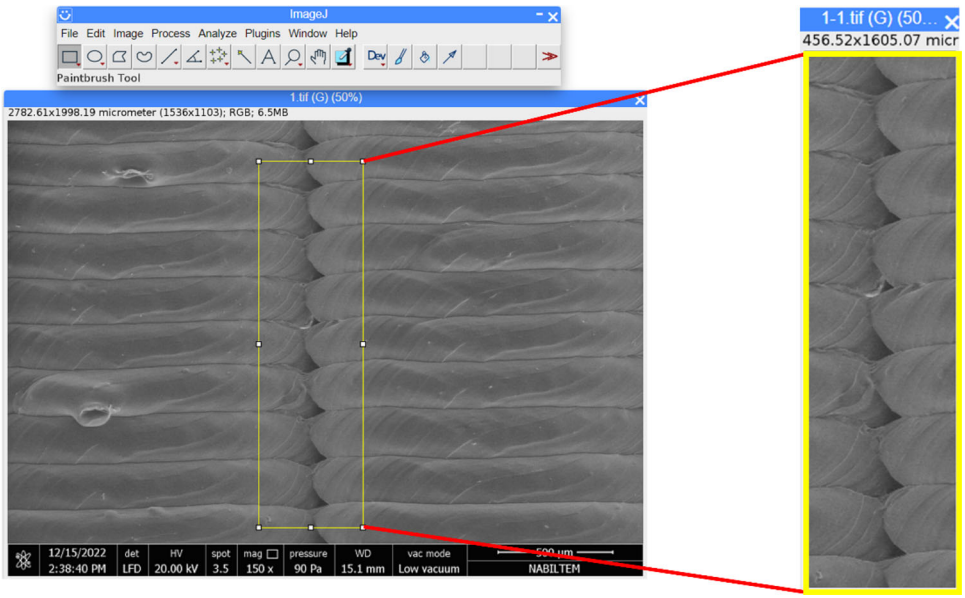


Fig. 10 SEM image processing (area selection for void density area calculation)

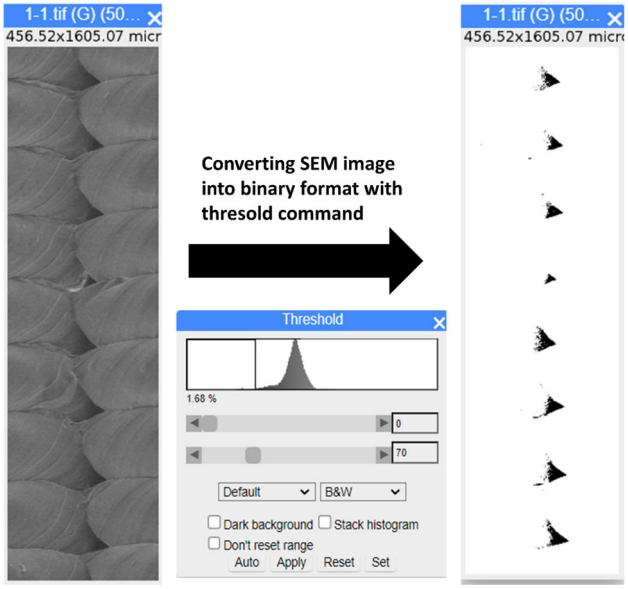


Fig. 11 SEM image processing (converting into binary format)

area densities are determined for each specimen by averaging calculated void areas. Theoretically, section of 3D printed tensile specimen with thickness of 3.2 mm and width of 6 mm which is produced with 0.8-mm nozzle has number of 105 void. Calculation steps for the determination of average void area density are shown in Fig. 12.

Sections perpendicular to tensile direction of FDM-printed nanocomposites are presented in Fig. 13. Interlayer adhesion is adequate in both reinforced and pure polymers as seen in SEM images. CNT reinforcement in ABS matrix has positive impact on porosity as depicted in Table 2. During 3D printing process, deposited fibers onto platform shrink due to sudden cooling [57]. Shrinkage has decreased on account of CNT reinforcement in ABS matrix.

3.3 Quasi-Static Tensile, Cyclic and Creep Tests

The stress–strain curves of FDM-printed ABS-CNT nanocomposites at 1E-3 strain rate are shown in Fig. 14. Effect of CNT reinforcement on the tensile strength, elastic modulus and strain at break are also presented as bar plots in Fig. 15. Variations in mechanical properties could be observed depending on the weight percentage of CNT reinforcement, as well as deformation rate and type of filler. It can be observed that the addition of CNT significantly affects the mechanical properties. In some cases, a decrease in elastic is observed for low levels of CNT reinforcement, likely due to insufficient interfacial adhesion between CNT and the polymer matrix. This issue diminishes as the amount of nanofiller increases. Multi-walled carbon nanotubes contribute to increased rigidity and strength of 3D printed parts due to their high specific surface area and aspect ratios.

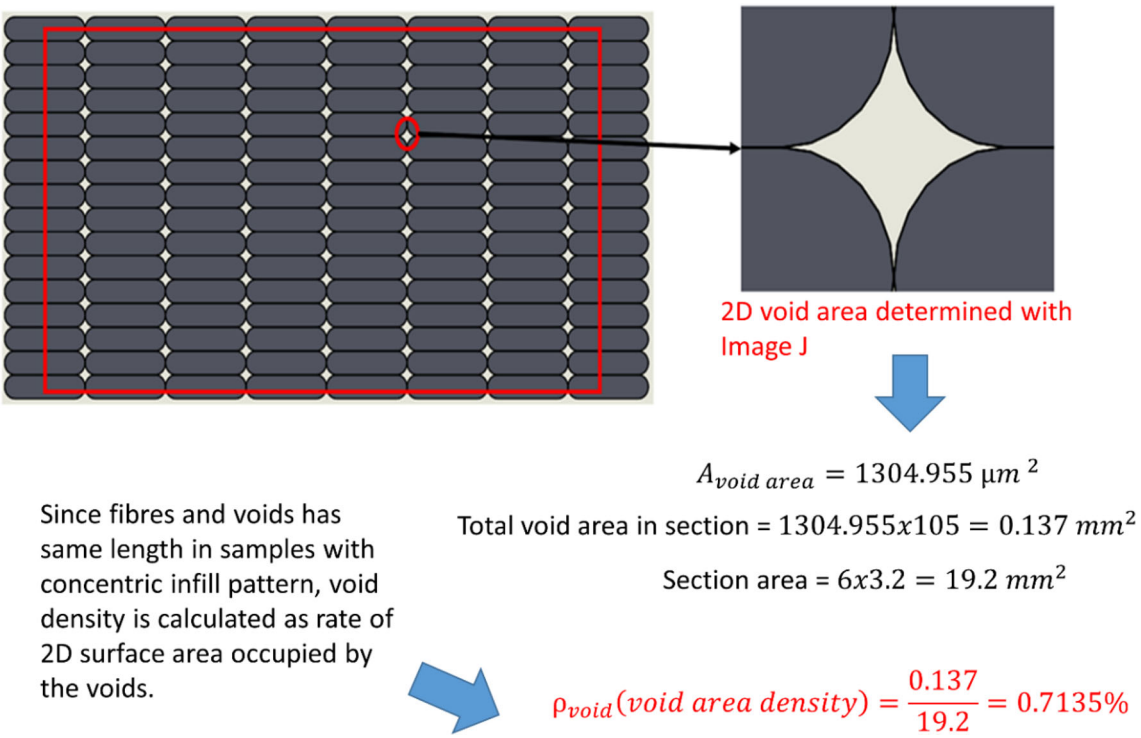


Fig. 12 Determination void area density

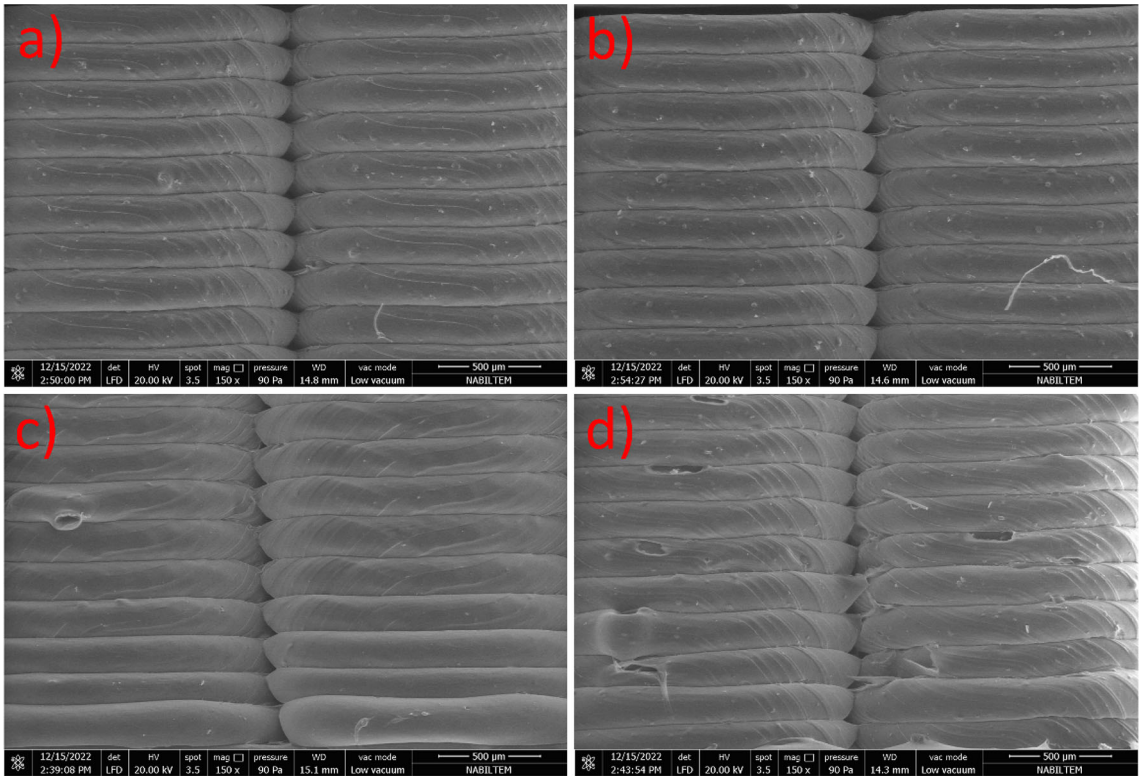


Fig. 13 SEM images of FDM-printed ABS-CNT nanocomposites, **a** Neat ABS, **b** ABS-wt%2CNT, **c** ABS-wt%4CNT, **d** ABS-wt%6CNT

Table 2 Void area densities of nanocomposite polymers

Material	Average single void section area (μm^2)	Total void area in section (mm^2)	Void area density (%)
Pure ABS	4034.141 ± 623.862	0.4236	2.2062
ABS-wt%2CNT	2946.783 ± 661.874	0.3094	1.6115
ABS-wt%4CNT	1756.463 ± 354.994	0.1844	0.9605
ABS-wt%6CNT	1681.242 ± 537.634	0.1765	0.9194

As mentioned before, the homogeneous dispersion of nanoparticles within the main polymer matrix is essential for the mechanical properties of parts produced with FDM. To achieve homogeneous dispersion, in addition to the melt blending process, a different approach from other methods in the literature is employed. It is considered that better adhesion between the polymer and nanoreinforcement could be achieved by pulverizing polymer granules into powder form using a pulverization machine (disk diameter: 500 mm, 55 kW motor, 5250 rpm). As seen in Fig. 15, different infill patterns has not significantly affected the tensile strength of ABS-CNT nanocomposites. In samples with a concentric infill pattern, the alignment of filaments during 3D printing is parallel to the tensile direction. This alignment contributes to a higher tensile strength compared to the line infill pattern, where the filaments make an angle of 45° with the tensile direction. In the concentric filler type, adjacent semi-molten filaments deposited on the platform have more contact surface due to adhesion, which is longer than in the line infill pattern. Different deformation rates partially influence the tensile strength. Tensile strength increase with an increase in deformation rate as shown in Fig. 15. The reinforcement of carbon nanotubes has significantly improved the tensile strengths of FDM-printed ABS. However, after a %wt4 CNT content, a decrease in tensile strength is observed in ABS-CNT samples. The decrease in tensile strength and elastic modulus at high reinforcement levels can be attributed to inappropriate carbon nanotube clustering. In the tensile tests conducted at a deformation rate of 1E-3, the tensile strengths of ABS-CNT samples with a concentric filler type have increased by approximately 14.61%, 49.14%, and 30.99% for weight percentages of %wt2, %wt4, and %wt6 CNT reinforcement, respectively.

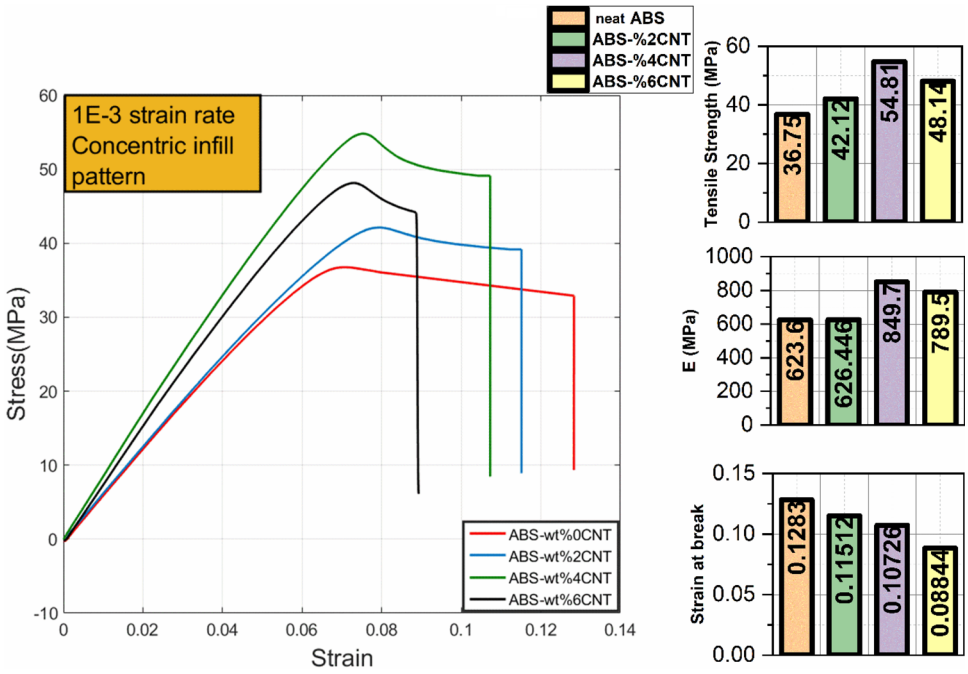


Fig. 14 Stress–strain graph at 1E-3 strain rate (concentric infill pattern)

The effect of nanoreinforcement on the elastic modulus of 3D printed nanocomposite parts are shown in Fig. 15. Similar to the tensile strength, there is an optimal CNT content of 4% by weight for ABS samples. Beyond this value, the elastic modulus starts to decrease. This is believed to be due to insufficient interfacial adhesion and CNT agglomeration, as discussed in the previous section. However, in general, the addition of CNTs increases the elastic modulus. This improvement can be attributed to the high specific surface area and aspect ratio of carbon nanotubes, as well as better adhesion between the layers of the composite materials, resulting in reduced pore density. The effect of deformation rate on the elastic modulus is not very pronounced. Rate-dependent mechanical behaviors are better demonstrated in loading–unloading tests. Under a deformation rate of 1E-3, the elastic modulus of ABS-CNT nanocomposites with line infill pattern increased by approximately 39.76%, 76.61%, and 51.02% for %wt2, %wt4, and %wt6 CNT-reinforced samples, respectively.

The strain rate-dependent recovery behaviors of 3D printed CNT-reinforced ABS materials in cyclic tests are shown in Figs. 16 and 17. At a strain level of 3%, ABS-CNT nanocomposites exhibited linear viscoelastic behavior. As the strain rate increased, an increase in the materials' strengths and stiffness is observed. As shown in Fig. 17, the amount of energy expended for deformation at a strain rate of 1E-3 is greater than that in tests performed at 1E-4 strain rate. When the strain rate is increased from 1E-4 to 1E-3, the amount of energy expended for deformation until reaching a 5% strain level increased in ABS matrix-based composites by approximately 7.74%, 1.58%, 1.07%, and 2.48% for materials reinforced with neat, %wt2, %wt4, and %wt6 CNTs, respectively.

During the recovery stage, polymer chains try to restore its initial form. Nevertheless, the degree and efficiency of this restoration process could be impacted by different parameters such as strain level and the duration of the allotted recovery time. When subjected to higher strain levels, reorganizing and reverting to their initial arrangement are more challenging for polymer chains [58]. This may lead to a prolonged and incomplete recovery process, resulting in more prominent decline in mechanical properties compared to samples subjected to lower strain levels. Besides, higher strain levels can induce more substantial harm to the polymer network, including chain scission or irreversible crosslinking [59]. At high strain rates, the molecular movements of polymer chains are restricted, and the time for chains to reorganize becomes shorter compared to low strain rates. Consequently, at high strain rates, there will be higher molecular resistance, leading to a more rigid behavior of the material [60]. As a result, in tests conducted at a strain rate of 1E-4, the elastic recovery after unloading is less compared to tests performed at 1E-3 strain rate (Fig. 17). When the strain rate decreases, the elastic recovery in ABS-CNT nanocomposites decreases by approximately 10.63%, 3.67%, 2.46%, and 4.79% for samples with neat, %wt2, %wt4, and %wt6 CNT content, respectively. After cyclic tests, a higher hysteresis (energy loss) is observed at low strain rates. This can again be attributed to the restricted movement of molecular chains at higher strain rates. The nanoreinforcement is seen to enhance the elastic

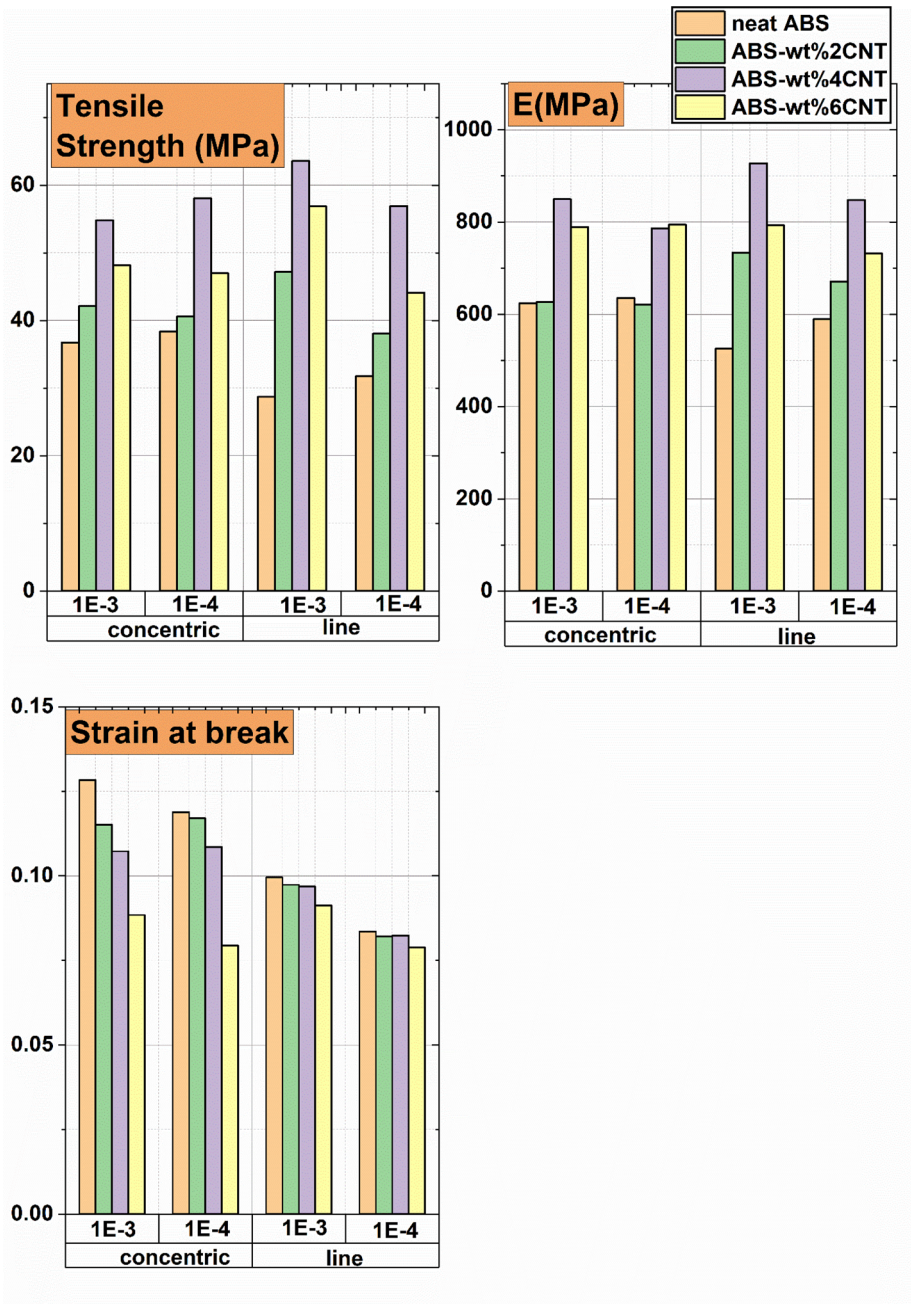


Fig. 15 Effect of CNT reinforcement on mechanical properties

recovery. This is believed to be a result of CNT reinforcement increasing the rigidity of the samples. In summary, at high strain rates, the materials exhibit increased molecular resistance and rigidity due to the constrained movements of polymer chains. The elastic recovery is higher at low strain rates, and the presence of nanoreinforcement enhances the materials' elastic recovery and rigidity.

Figures 18 depicts time-dependent creep compliance curves obtained from creep tests conducted on FDM-printed nanoreinforced ABS materials. The tests are conducted at room temperature under a constant stress of 16.25 MPa for approximately 2.78 h. To achieve the desired stress level, an instantaneous load is applied, resulting in rapid deformation due to elastic or instantaneous creep [61].

The inclusion of CNT as reinforcement clearly promotes the reduction of creep compliance in every infill type. The nanofiller plays an important role in limiting the mobility of the polymer chains, thereby fostering improved creep stability. Polymers exhibit creep strain at relatively low stresses, even at room temperatures. The origin of creep in polymers lies in the delayed response exhibited by polymer chains.

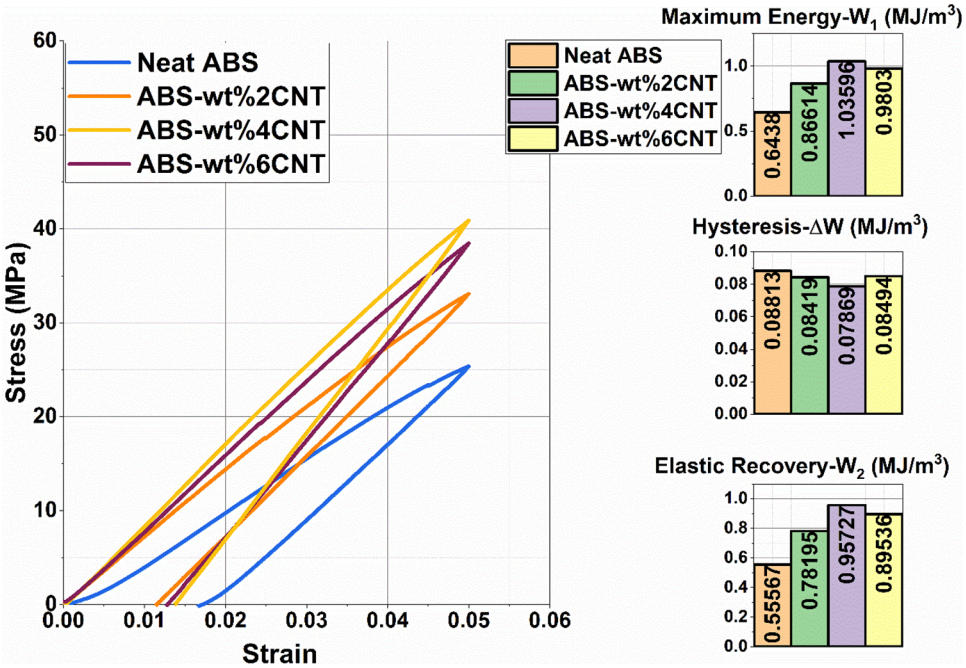


Fig. 16 Cyclic loading test at 1E-4 strain rate and %5 strain level (concentric infill pattern)

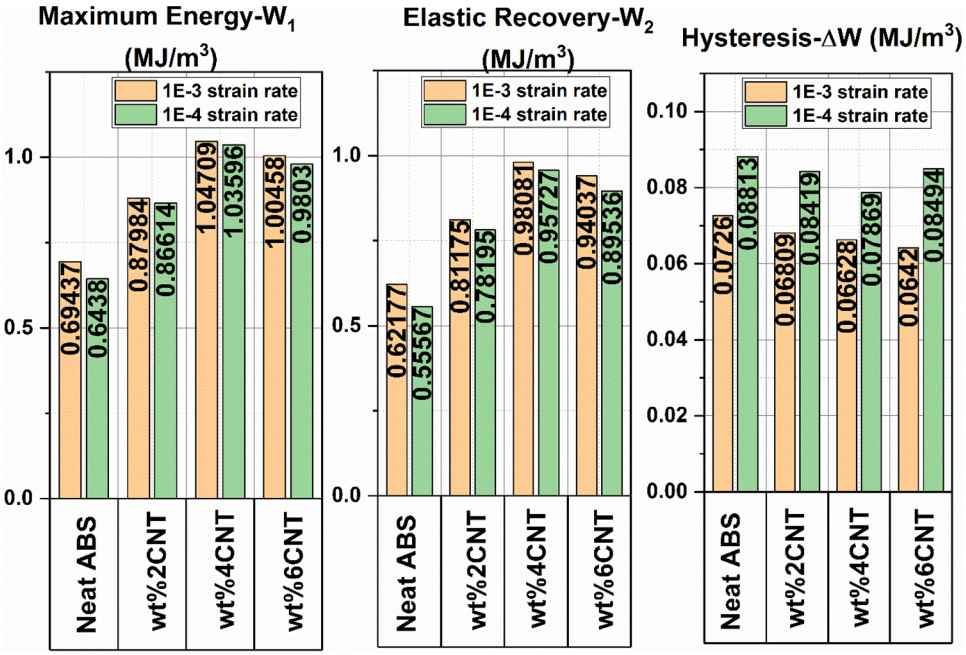


Fig. 17 Strain rate-dependent recovery behavior

Stress level in relation to the yield point of the polymer significantly influences the creep response. Low stress values may result in the occurrence of primary and secondary creep, whereas stress levels near the yield point can trigger primary creep, along with brief secondary and tertiary creep [62]. As shown in Fig. 18 and Table 3, unfilled polymers exhibit higher total creep deformation compared to those reinforced polymers. Creep tests conducted on 3D printed ABS-CNT nanocomposites with line infill pattern show a reduction in isothermal creep compliances of 0.97%, 28.66%, and 17.18% for materials reinforced with %wt2, %wt4, and %wt6 nanofillers, respectively. The results are coincided with the tensile and cyclic tests, indicating that the nanocomposites with a 4% weight fraction of nanofillers exhibited better creep performance compared to other filler ratios. Although there may be exceptions in the time-dependent viscoelastic creep compliances due to CNT agglomeration and insufficient interfacial adhesion, an overall reduction is observed with nanofillers, indicating the beneficial effect of CNT reinforcement. In summary, the presence of nanofillers in the

Fig. 18 Creep test results

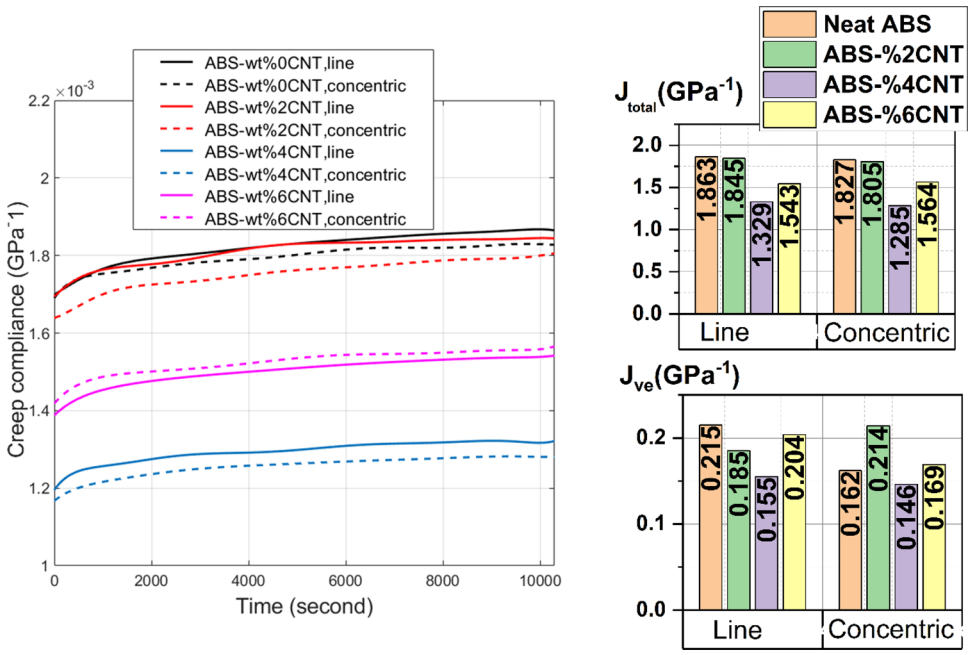


Table 3 Creep compliances

Material	Line infill pattern			Concentric infill pattern		
	J_{el} (GPa^{-1})	J_{ve} (GPa^{-1})	J_{total} (GPa^{-1})	J_{el} (GPa^{-1})	J_{ve} (GPa^{-1})	J_{top} (GPa^{-1})
Pure ABS	1.648	0.215	1.863	1.665	0.162	1.827
ABS-wt%2CNT	1.66	0.185	1.845	1.591	0.214	1.805
ABS-wt%4CNT	1.174	0.155	1.329	1.139	0.146	1.285
ABS-wt%6CNT	1.339	0.204	1.543	1.395	0.169	1.564

polymer matrix leads to reduced creep deformation, and CNT reinforcement generally improves the creep performance of the materials. The results are consistent with other mechanical tests, and nanocomposites with a 4% weight fraction of nanofillers exhibit the best creep performance.

3.4 NARX, Transfer Function and Process Model Simulations

The model structures for uniaxial tensile test process and cyclic test process are generated as shown in Fig. 19. Here, "ρ" represents the void area density, "$\dot{\varepsilon}$" denotes the strain rate, "σ" represents the applied stress during the test, and "ε" represents the strain response of the system. It can be stated that the void area density of the samples decrease during the tensile test due to cross-sectional waisting. To ensure more accurate characterization, the cross-sectional areas of the samples are measured both before and after each tensile test. By comparing the cross-sectional areas before and after the test, the changes in void area density are determined, assuming that these changes decrease linearly over time.

Model structure for tensile test is developed using data obtained from tests at strain rates of 1E-3 and 1E-4 for ABS-%wt4 CNT samples, as well as for ABS-%wt6 CNT samples at the same strain rates. To validate the generated model, test data from pure ABS samples at strain rates of 1E-3 and 1E-4, and ABS-%wt2 CNT samples at the same strain rates are utilized. The model parameters and results for tensile test process and cyclic test process are presented in Table 4. To compare models and experimental data, stress–strain graphs for tensile test process is presented in Fig. 20.

Model structure for cyclic tests is developed using experimental data obtained from pure ABS and ABS-%wt2CNT samples. For validation, the experimental data from ABS-%wt4CNT and ABS-%wt6CNT samples are utilized. However, while sigmoid activation function is used in other models, here the wavelet activation function is preferred. The wavelet function performs better in cases where the output response exhibits sudden changes. The model parameters and results for tensile test process and cyclic test process are presented in Table 5. To compare models and experimental

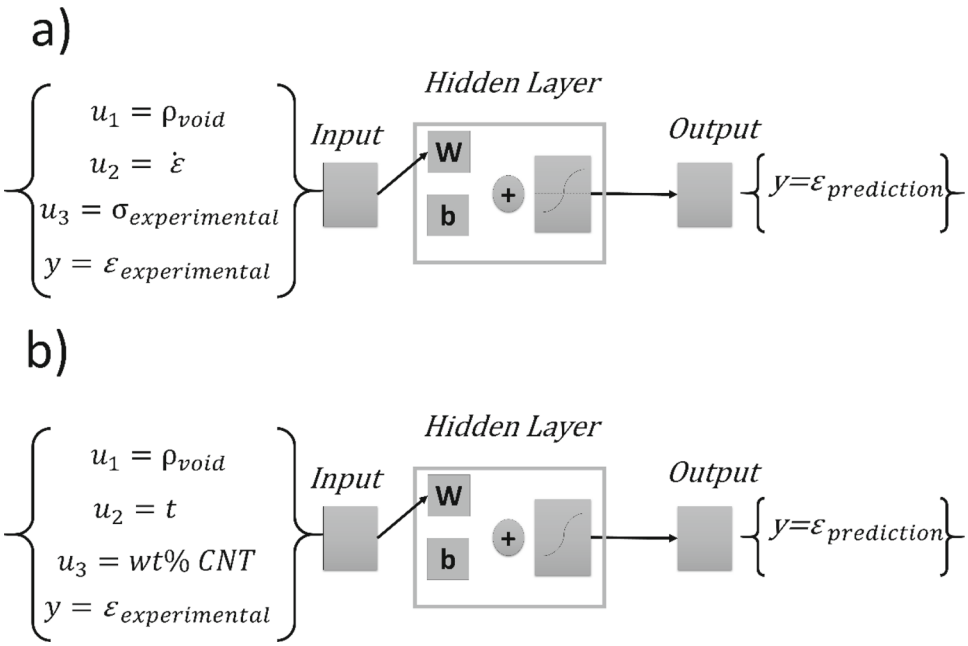


Fig. 19 Model structures; **a** quasi-static tensile and cyclic test process, **b** creep test process

Table 4 Estimated model parameters for quasi-static tensile test process

Estimation data	Model	Fit to estimation data	Fit to validation data
ABS-wt%4CNT @ 1E-3 ABS-wt%4CNT @ 1E-4 ABS-wt%6CNT @ 1E-3 ABS-wt%6CNT @ 1E-4	*Transfer function model* $u_1 \rightarrow y$ $G(s) = \frac{-4.979x10^{-7}}{s+0.0003831}$ $u_2 \rightarrow y$ $G(s) = \frac{0.04087}{s+0.0004159}$ $u_3 \rightarrow y$ $G(s) = \frac{0.0001136}{s+0.001472}$	ABS-wt%4CNT @ 1E-3 **87.37%** ABS-wt%4CNT @ 1E-4 **88.98%** ABS-wt%6CNT @ 1E-3 **84.82%** ABS-wt%6CNT @ 1E-4 **88.24%**	Neat ABS @ 1E-3 **80.01%** Neat ABS @ 1E-4 **77.97%** ABS-wt%2CNT @ 1E-3 **78.45%** ABS-wt%2CNT @ 1E-4 **75.43%**
ABS-wt%4CNT @ 1E-3 ABS-wt%4CNT @ 1E-4 ABS-wt%6CNT @ 1E-3 ABS-wt%6CNT @ 1E-4	*Process model* $u_1 \rightarrow y$ $G(s) = \frac{-0.0011394}{1+281.16s} e^{30s}$ $u_2 \rightarrow y$ $G(s) = \frac{-391.04}{1+4561.1s} e^{0.001s}$ $u_3 \rightarrow y$ $G(s) = \frac{0.45983}{1+4507.5s} e^{30s}$	ABS-wt%4CNT @ 1E-3 **83.33%** ABS-wt%4CNT @ 1E-4 **81.97%** ABS-wt%6CNT @ 1E-3 **83.02%** ABS-wt%6CNT @ 1E-4 **84.59%**	Neat ABS @ 1E-3 **74.96%** Neat ABS @ 1E-4 **74.01%** ABS-wt%2CNT @ 1E-3 **72.85%** ABS-wt%2CNT @ 1E-4 **70.31%**
ABS-wt%4CNT @ 1E-3 ABS-wt%4CNT @ 1E-4 ABS-wt%6CNT @ 1E-3 ABS-wt%6CNT @ 1E-4	*NARX Model* *Activation function:* Sigmoid with 2 neuron *Optimization algorithm:* Levenberg–Marquardt	ABS-wt%4CNT @ 1E-3 **94.36%** ABS-wt%4CNT @ 1E-4 **94.01%** ABS-wt%6CNT @ 1E-3 **97.06%** ABS-wt%6CNT @ 1E-4 **96.7%**	Neat ABS @ 1E-3 **85.56%** Neat ABS @ 1E-4 **87.01%** ABS-wt%2CNT @ 1E-3 **90.71%** ABS-wt%2CNT @ 1E-4 **86.61%**

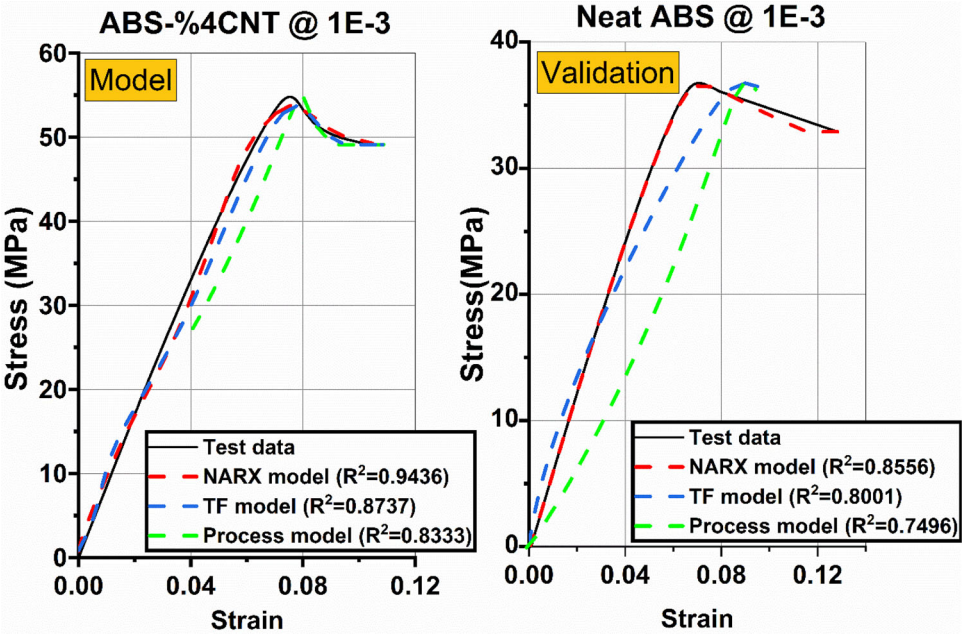


Fig. 20 Tensile test model and validation results

Table 5 Estimated model parameters for cyclic test process

Estimation data	Model	Fit to estimation data	Fit to validation data
Neat ABS @ 1E-3 Neat ABS @ 1E-4 ABS-wt%2CNT @ 1E-3 ABS-wt%2CNT @ 1E-4	*Transfer function model* $u_1 \rightarrow y$ $G(s) = \frac{0.0009209s+7.483x10^{-5}}{s^2+0.4482s+0.0529}$ $u_2 \rightarrow y$ $G(s) = \frac{0.6756s+0.003518}{s^2+0.09891s+0.0005364}$ $u_3 \rightarrow y$ $G(s) = \frac{-0.0003067-2.466x10^{-6}}{s^2+0.1036s+0.0008058}$	Neat ABS @ 1E-3 **81.33%** Neat ABS @ 1E-4 **83.6%** ABS-wt%2CNT @ 1E-3 **79.98%** ABS-wt%2CNT @ 1E-4 **84.2%**	ABS-wt%4CNT @ 1E-3 **73.84%** ABS-wt%4CNT @ 1E-4 **72.13%** ABS-wt%6CNT @ 1E-3 **71.12%** ABS-wt%6CNT @ 1E-4 **74.42%**
Neat ABS @ 1E-3 Neat ABS @ 1E-4 ABS-wt%2CNT @ 1E-3 ABS-wt%2CNT @ 1E-4	*Process model* $u_1 \rightarrow y$ $G(s) = \frac{0.29103}{1+1.7164x10^{-7}s} e^{-0.01s}$ $u_2 \rightarrow y$ $G(s) = \frac{-3.7607}{1+9080.1s} e^{7.867s}$ $u_3 \rightarrow y$ $G(s) = \frac{-0.0019469}{1+9902.9s} e^{7.867s}$	Neat ABS @ 1E-3 **72.77%** Neat ABS @ 1E-4 **74.68%** ABS-wt%2CNT @ 1E-3 **69.82%** ABS-wt%2CNT @ 1E-4 **74.62%**	ABS-wt%4CNT @ 1E-3 **65.13%** ABS-wt%4CNT @ 1E-4 **63.57%** ABS-wt%6CNT @ 1E-3 **67.06%** ABS-wt%6CNT @ 1E-4 **62.01%**
Neat ABS @ 1E-3 Neat ABS @ 1E-4 ABS-wt%2CNT @ 1E-3 ABS-wt%2CNT @ 1E-4	*NARX Model* *Activation function:* Wavelet with 2 neuron *Optimization algorithm:* Levenberg–Marquardt	Neat ABS @ 1E-3 **97.57%** Neat ABS @ 1E-4 **98.73%** ABS-wt%2CNT @ 1E-3 **98.01%** ABS-wt%2CNT @ 1E-4 **98.70%**	ABS-wt%4CNT @ 1E-3 **87.48%** ABS-wt%4CNT @ 1E-4 **90.37%** ABS-wt%6CNT @ 1E-3 **89.65%** ABS-wt%6CNT @ 1E-4 **90.35%**

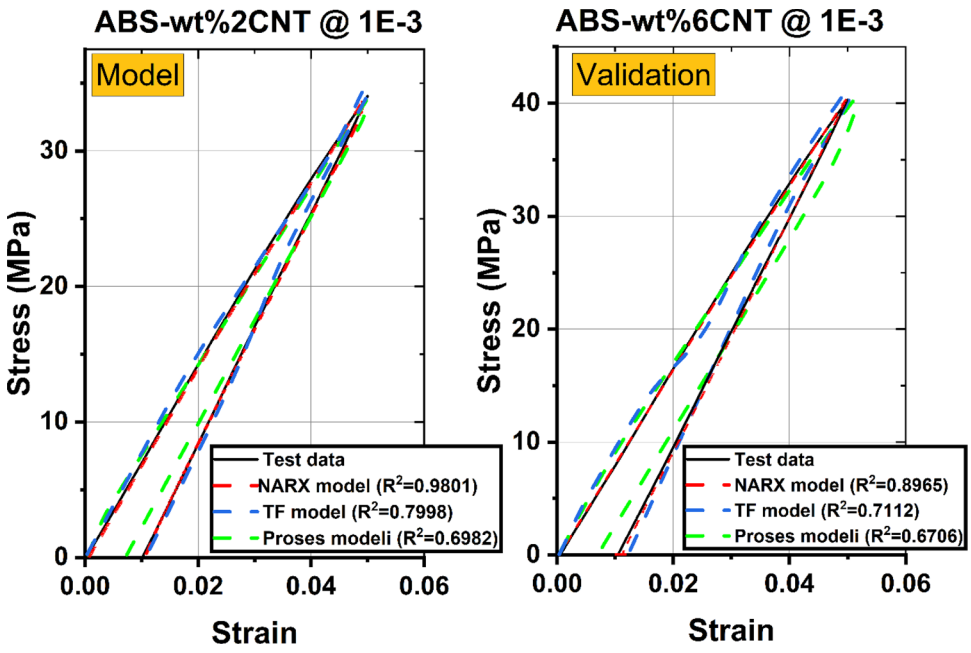


Fig. 21 Cyclic test model and validation results

Table 6 Estimated model parameters for creep test process

Estimation data	Model	Fit to estimation data	Fit to validation data
Neat ABS ABS-wt%2CNT	*Transfer function model* $u_1 \rightarrow y$ $G(s) = \frac{8.403x10^{-5}s+4.303x10^{-13}}{s^2+0.008675s+3.288x10^{-6}}$ $u_2 \rightarrow y$ $G(s) = \frac{-0.002518s-2.168x10^{-8}}{s^2+0.0003637s+3.094x10^{-9}}$ $u_3 \rightarrow y$ $G(s) = \frac{2.722x10^{-5}s+1.897x10^{-7}}{s^2+0.009075s+3.496x10^{-6}}$	Neat ABS **85.03%** ABS-wt%2CNT **88.38%**	ABS-wt%4CNT **77.48%** ABS-wt%6CNT **80.97%**
Neat ABS @ ABS-wt%2CNT @	*Process model* $u_1 \rightarrow y$ $G(s) = \frac{1.8922x10^{-7}}{1+14.377s} e^{-0.065s}$ $u_2 \rightarrow y$ $G(s) = \frac{12.812}{1+1911.1s} e^{-1.766s}$ $u_3 \rightarrow y$ $G(s) = \frac{-0.14192}{1+1957.9s} e^{-0.001s}$	Neat ABS **78.79%** ABS-wt%2CNT @ **77.92%**	ABS-wt%4CNT **72.20%** ABS-wt%6CNT **72.55%**
Neat ABS @ ABS-wt%2CNT @	*NARX model* *Activation function:* Sigmoid with 1 neuron *Optimization algorithm:* Levenberg–Marquardt	Neat ABS **90.81%** ABS-wt%2CNT **91.32%**	ABS-wt%4CNT **87.92%** ABS-wt%6CNT **88.13%**

data stress–strain graphs for loading–unloading test process is presented in Fig. 21.

Since the creep test is conducted at a specific constant stress level, and it is an independent experiment from strain rate, the strain rate is not taken as an input variable. The input variables for the model are time (s), CNT content (%wt), and void area density (ρ_{void}), while the output variable is strain (ε). The data from pure ABS and ABS-%wt2 CNT

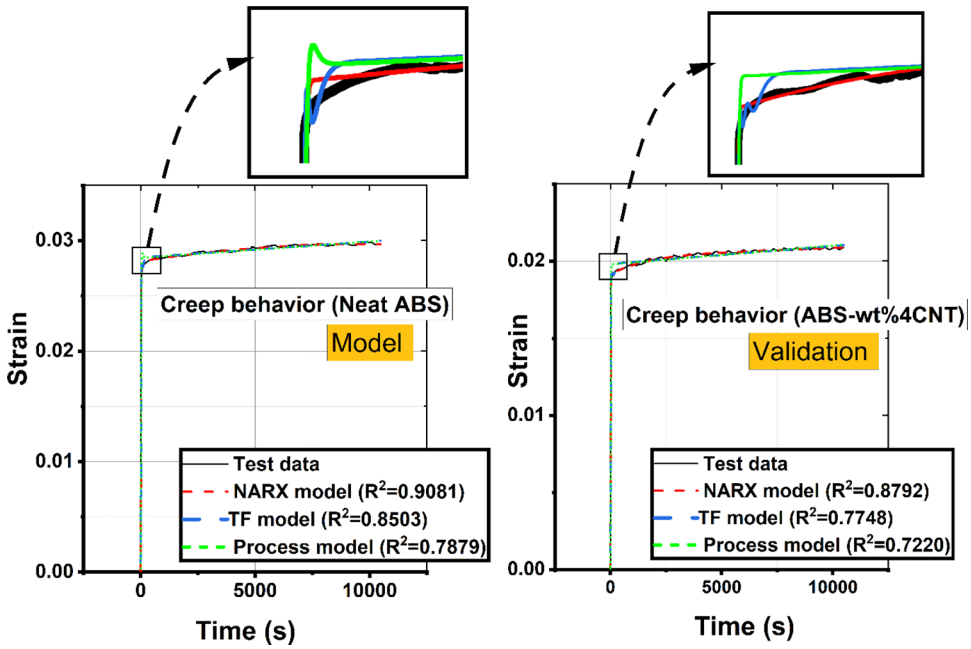


Fig. 22 Creep test model and validation results

samples are used to construct the model, and the data from ABS-%wt4 CNT and ABS-%wt6 CNT samples are used for validation. The model parameters and results are given in Table 6. The creep tests are performed under a constant stress of 16.25 MPa. Due to the small fluctuations experienced while attempting to maintain the sample under this stress level in the testing device, the strain–time curve is not linear. As a result, the agreement between the experimental data and the model is lower compared to other processes. To compare models and experimental data, stress–strain graphs for creep test process are presented in Fig. 22.

4 Conclusion

In this study, nanocomposite filaments of ABS-CNT with different amounts of carbon nanotube reinforcement are produced to use in 3D printing. The thermal degradation behaviors of the produced filaments are investigated through thermogravimetric analysis and differential scanning calorimetry. Samples fabricated using nanocomposite filaments are subjected to tensile, loading–unloading and creep tests to determine and characterize their mechanical behaviors concerning time and strain rate. The porosity of the 3D printed samples is determined using SEM images and ImageJ software to investigate the effects of nanoreinforcement on the porosity of the produced samples. For modeling the mechanical and behaviors of the produced nanocomposites, linear transfer functions and process models, as well as nonlinear autoregressive exogenous (NARX) models, are proposed. Multi-input, single-output structures are established for the mechanical test processes in the modeling. The results obtained from the study can be summarized as follows:

- The weight percentages of CNTs in the produced nanocomposite filaments are determined using TGA (thermogravimetric analysis) analyses. The TGA analyses are performed at different temperatures, specifically at 450 °C, 475 °C, and 500 °C for ABS-CNT filaments. The data obtained from these TGA analyses demonstrated that the achieved weight percentages of CNTs in the filaments are close to the desired levels at a sufficient degree of accuracy.
- When examining the SEM images of samples produced with concentric filler type, it can be stated that both pure and CNT-reinforced samples exhibit sufficient interlayer adhesion. As the CNT reinforcement content increases, the adhesion between filaments improves, and the size of pores decreases. During 3D printing, rapid cooling may cause shrinkage, leading to inadequate adhesion between filament strands. However, this issue is overcome by CNT reinforcement. Void area densities are decreased by approximately 26.94%, 56.45%, and 58.32%, respectively, with 2 wt%, 4 wt%, and 6 wt% CNT content.
- The addition of CNTs improved the mechanical properties. In the tests conducted at a strain rate of 1E-3, ABS samples with concentric infill pattern, the tensile strength increased by approximately 14.61%, 49.14%, and 30.99% with %wt2, %wt4, and %wt6 CNT content, respectively.
- The results from the load–unload tests indicate that ABS-CNT nanocomposite materials exhibit linear viscoelastic behavior. As the strain rate increases, an increase in material strength is observed. The energy expended for

deformation at a strain rate of 1E-3 is higher than that in tests conducted at 1E-4 strain rate. CNT reinforcement has increased the stiffness of the materials. With 2 wt%, 4 wt%, and 6 wt% CNT content, the average energy expended to reach a 5% strain level in ABS samples increases by approximately 26.71%, 50.79%, and 44.67%, respectively, at a strain rate of 1E-3.

- In creep tests, a decrease in creep compliance is observed in ABS-CNT nanocomposites with the addition of nanoreinforcement. The creep compliances decrease by approximately 0.97%, 28.66%, and 17.17% for 2 wt%, 4 wt%, and 6 wt% CNT reinforcements, respectively. Although there may be exceptions due to CNT agglomerations and insufficient interfacial adhesion, the overall trend shows a decrease in viscoelastic creep compliance with the addition of nanoreinforcement, indicating the positive effect of CNT reinforcement on the creep behavior of the nanocomposites.
- System identification is employed to create both linear and nonlinear models, and particularly, the nonlinear NARX model effectively modeled the mechanical behaviors of the nanocomposite polymers produced via FDM with high accuracy. While the activation function used in the model structures is generally the sigmoid function, the wavelet activation function exhibited superior performance in the loading–unloading test process. When there are sudden changes in the output variables, the wavelet activation function outperformed the sigmoid function, providing more accurate and reliable results.

Funding Open access funding provided by the Scientific and Technological Research Council of Türkiye (TÜBİTAK).

Declarations

Conflict of interest The authors declare that they have no conflicts of interest regarding this article.

Open Access This article is licensed under a Creative Commons Attribution 4.0 International License, which permits use, sharing, adaptation, distribution and reproduction in any medium or format, as long as you give appropriate credit to the original author(s) and the source, provide a link to the Creative Commons licence, and indicate if changes were made. The images or other third party material in this article are included in the article's Creative Commons licence, unless indicated otherwise in a credit line to the material. If material is not included in the article's Creative Commons licence and your intended use is not permitted by statutory regulation or exceeds the permitted use, you will need to obtain permission directly from the copyright holder. To view a copy of this licence, visit http://creativecommons.org/licenses/by/4.0/.

References

1. Tymrak, B.M.; Kreiger, M.; Pearce, J.M.: Mechanical properties of components fabricated with open-source 3-D printers under realistic environmental conditions. Mater. Des. **58**, 242–246 (2014). https://doi.org/10.1016/j.matdes.2014.02.038
2. Ning, F.; Cong, W.; Hu, Y.; Wang, H.: Additive manufacturing of carbon fiber-reinforced plastic composites using fused deposition modeling: Effects of process parameters on tensile properties. J. Compos. Mater. **51**(4), 451–462 (2017). https://doi.org/10.1177/0021998316646169
3. Hegab, H.A.: Design for additive manufacturing of composite materials and potential alloys: a review. Manuf. Rev. **3**, 11 (2016). https://doi.org/10.1051/mfreview/2016010
4. Tekinalp, H.L., et al.: Highly oriented carbon fiber–polymer composites via additive manufacturing. Compos. Sci. Technol. **105**, 144–150 (2014). https://doi.org/10.1016/j.compscitech.2014.10.009
5. Lee, B.H.; Abdullah, J.; Khan, Z.A.: Optimization of rapid prototyping parameters for production of flexible ABS object. J. Mater. Process. Technol. **169**(1), 54–61 (2005). https://doi.org/10.1016/j.jmatprotec.2005.02.259
6. Prashantha, K.; Roger, F.: Multifunctional properties of 3D printed poly(lactic acid)/graphene nanocomposites by fused deposition modeling. J. Macromol. Sci. Part A **54**(1), 24–29 (2017). https://doi.org/10.1080/10601325.2017.1250311
7. Zhong, W.; Li, F.; Zhang, Z.; Song, L.; Li, Z.: Short fiber reinforced composites for fused deposition modeling. Mater. Sci. Eng. A **301**(2), 125–130 (2001). https://doi.org/10.1016/S0921-5093(00)01810-4
8. Ahn, S.H.; Montero, M.; Odell, D.; Roundy, S.; Wright, P.K.: Anisotropic material properties of fused deposition modeling ABS. Rapid Prototyp. J. **8**(4), 248–257 (2002). https://doi.org/10.1108/13552540210441166
9. Es-Said, O.S.; Foyos, J.; Noorani, R.; Mendelson, M.; Marloth, R.; Pregger, B.A.: Effect of layer orientation on mechanical properties of rapid prototyped samples. Mater. Manuf. Process. **15**(1), 107–122 (2000). https://doi.org/10.1080/10426910008912976
10. Croccolo, D.; De Agostinis, M.; Olmi, G.: Experimental characterization and analytical modelling of the mechanical behaviour of fused deposition processed parts made of ABS-M30. Comput. Mater. Sci. **79**, 506–518 (2013). https://doi.org/10.1016/j.commatsci.2013.06.041
11. Dawoud, M.; Taha, I.; Ebeid, S.J.: Effect of processing parameters and graphite content on the tribological behaviour of 3D printed acrylonitrile butadiene styrene. Mater. Werkst. **46**(12), 1185–1195 (2015). https://doi.org/10.1002/mawe.201500450
12. Panda, S.K.; Padhee, S.; Sood, A.K.; Mahapatra, S.S.: Optimization of fused deposition modelling (FDM) process parameters using bacterial foraging technique. Intell. Inf. Manag. **01**(02), 89 (2009). https://doi.org/10.4236/iim.2009.12014
13. Melenka, G.W.; Schofield, J.S.; Dawson, M.R.; Carey, J.P.: Evaluation of dimensional accuracy and material properties of the MakerBot 3D desktop printer. Rapid Prototyp. J. **21**(5), 618–627 (2015). https://doi.org/10.1108/RPJ-09-2013-0093
14. Torres, J.; Cotelo, J.; Karl, J.; Gordon, A.P.: Mechanical property optimization of FDM PLA in shear with multiple objectives. JOM **67**(5), 1183–1193 (2015). https://doi.org/10.1007/s11837-015-1367-y
15. M. Berber and I. H. Hafez, *Carbon nanotubes: current progress of their polymer composites*. BoD – Books on Demand, 2016
16. Dul, S.; Fambri, L.; Pegoretti, A.: Fused deposition modelling with ABS–graphene nanocomposites. Compos. Part Appl. Sci. Manuf. **85**, 181–191 (2016). https://doi.org/10.1016/j.compositesa.2016.03.013

17. Bustillos, J.; Montero, D.; Nautiyal, P.; Loganathan, A.; Boesl, B.; Agarwal, A.: Integration of graphene in poly(lactic) acid by 3D printing to develop creep and wear-resistant hierarchical nanocomposites. Polym. Compos. **39**(11), 3877–3888 (2018). https://doi.org/10.1002/pc.24422
18. Zhang, D., et al.: Fabrication of highly conductive graphene flexible circuits by 3D printing. Synth. Met. **217**, 79–86 (2016). https://doi.org/10.1016/j.synthmet.2016.03.014
19. Fu, K.; Yao, Y.; Dai, J.; Hu, L.: Progress in 3D printing of carbon materials for energy-related applications. Adv. Mater. **29**(9), 1603486 (2017). https://doi.org/10.1002/adma.201603486
20. Uranbey, L.; Unal, H.I.; Calis, G.; Gumus, O.Y.; Katmer, S.; Karatas, C.: One-pot preparation of electroactive shape memory polyurethane/carbon black blend. J. Mater. Eng. Perform. **30**(3), 1665–1673 (2021). https://doi.org/10.1007/s11665-021-05461-5
21. Ashok Gandhi, R.; Palanikumar, K.; Ragunath, B.K.; Paulo Davim, J.: Role of carbon nanotubes (CNTs) in improving wear properties of polypropylene (PP) in dry sliding condition'. Mater. Des. **48**, 52–57 (2013). https://doi.org/10.1016/j.matdes.2012.08.081
22. Ghoshal, S.: Polymer/carbon nanotubes (CNT) nanocomposites processing using additive manufacturing (three-dimensional printing) technique: an overview. Fibers **5**(4), 4 (2017). https://doi.org/10.3390/fib5040040
23. Gonzalez, G., et al.: Development of 3D printable formulations containing CNT with enhanced electrical properties. Polymer **109**, 246–253 (2017). https://doi.org/10.1016/j.polymer.2016.12.051
24. Mohamed, O.A.; Masood, S.H.; Bhowmik, J.L.: Influence of processing parameters on creep and recovery behavior of FDM manufactured part using definitive screening design and ANN. Rapid Prototyp. J. **23**(6), 998–1010 (2017). https://doi.org/10.1108/RPJ-12-2015-0198
25. Zhang, H., et al.: Tensile, creep, and fatigue behaviors of 3D-printed acrylonitrile butadiene styrene. J. Mater. Eng. Perform. **27**(1), 57–62 (2018). https://doi.org/10.1007/s11665-017-2961-7
26. Niaza, K.V.; Senatov, F.S.; Stepashkin, A.; Anisimova, N.Y.; Kiselevsky, M.V.: Long-term creep and impact strength of biocompatible 3D-printed PLA-based scaffolds. Nano Hybrids Compos. **13**, 15–20 (2017). https://doi.org/10.4028/www.scientific.net/NHC.13.15
27. Istif, I.; Feratoglu, K.; Colak, O.U.; Acar, A.: Investigation of tensile, viscoelastic, and viscoplastic behavior of polylactic acid manufactured by fused deposition modeling. J. Test. Eval. **49**(4), 2831–2839 (2021). https://doi.org/10.1520/JTE20180964
28. Yin, Z.N.; Fan, L.F.; Wang, T.J.: Experimental investigation of the viscoelastic deformation of PC, ABS and PC/ABS alloys. Mater. Lett. **62**(17), 2750–2753 (2008). https://doi.org/10.1016/j.matlet.2008.01.041
29. Mohamed, O.A.; Masood, S.H.; Bhowmik, J.L.: Experimental investigation of time-dependent mechanical properties of PC-ABS prototypes processed by FDM additive manufacturing process. Mater. Lett. **193**, 58–62 (2017). https://doi.org/10.1016/j.matlet.2017.01.104
30. Dakshinamurthy, D.; Gupta, S.: A study on the influence of process parameters on the viscoelastic properties of ABS components manufactured by FDM process. J. Inst. Eng. India Ser. C **99**(2), 133–138 (2018). https://doi.org/10.1007/s40032-016-0324-z
31. Istif, I.; Isin, O.; Uzunsoy, E.; Uzunsoy, D.: Non-linear modelling of PM brake lining wear behaviour. Mater. Test. **54**(1), 45–48 (2012). https://doi.org/10.3139/120.110295
32. Peng, A.; Xiao, X.; Yue, R.: Process parameter optimization for fused deposition modeling using response surface methodology combined with fuzzy inference system. Int. J. Adv. Manuf. Technol. **73**(1–4), 87–100 (2014). https://doi.org/10.1007/s00170-014-5796-5
33. Sood, A.K.; Ohdar, R.K.; Mahapatra, S.S.: Experimental investigation and empirical modelling of FDM process for compressive strength improvement. J. Adv. Res. **3**(1), 81–90 (2012). https://doi.org/10.1016/j.jare.2011.05.001
34. Xu, C.; Feng, H.; Li, Y.; Li, L.: Design of surpassing damping and modulus nanocomposites with tunable frequency range via hierarchical bio-architecture'. Polym. Compos. (2023). https://doi.org/10.1002/pc.28067
35. Xu, C.; Li, L.: A surpassingly stiff yet lossy multiscale nanocomposite inspired by bio-architecture. Mater. Today Commun. **35**, 105982 (2023). https://doi.org/10.1016/j.mtcomm.2023.105982
36. Uchida, T.; Kumar, S.: Single wall carbon nanotube dispersion and exfoliation in polymers. J. Appl. Polym. Sci. **98**(3), 985–989 (2005). https://doi.org/10.1002/app.22203
37. de Heer, W.A.: Nanotubes and the pursuit of applications. MRS Bull. **29**(4), 281–285 (2004). https://doi.org/10.1557/mrs2004.81
38. Cooper, C.A.; Young, R.J.; Halsall, M.: Investigation into the deformation of carbon nanotubes and their composites through the use of Raman spectroscopy. Compos. Part Appl. Sci. Manuf. **32**(3), 401–411 (2001). https://doi.org/10.1016/S1359-835X(00)00107-X
39. Frogley, M.D.; Ravich, D.; Wagner, H.D.: Mechanical properties of carbon nanoparticle-reinforced elastomers. Compos. Sci. Technol. **63**(11), 1647–1654 (2003). https://doi.org/10.1016/S0266-3538(03)00066-6
40. Postiglione, G.; Natale, G.; Griffini, G.; Levi, M.; Turri, S.: Conductive 3D microstructures by direct 3D printing of polymer/carbon nanotube nanocomposites via liquid deposition modeling. Compos. Part Appl. Sci. Manuf. **76**, 110–114 (2015). https://doi.org/10.1016/j.compositesa.2015.05.014
41. Farahani, R.D., et al.: Direct-write fabrication of freestanding nanocomposite strain sensors. Nanotechnology **23**(8), 085502 (2012). https://doi.org/10.1088/0957-4484/23/8/085502
42. Guo, S.; Yang, X.; Heuzey, M.-C.; Therriault, D.: 3D printing of a multifunctional nanocomposite helical liquid sensor. Nanoscale **7**(15), 6451–6456 (2015). https://doi.org/10.1039/C5NR00278H
43. Wang, P.-H.; Ghoshal, S.; Gulgunje, P.; Verghese, N.; Kumar, S.: Polypropylene nanocomposites with polymer coated multiwall carbon nanotubes. Polymer **100**, 244–258 (2016). https://doi.org/10.1016/j.polymer.2016.07.070
44. Kong, Y.; Yuan, J.; Wang, Z.; Qiu, J.: Study on the preparation and properties of aligned carbon nanotubes/polylactide composite fibers. Polym. Compos. **33**(9), 1613–1619 (2012). https://doi.org/10.1002/pc.22298
45. Ghoshal, S.; Wang, P.-H.; Gulgunje, P.; Verghese, N.; Kumar, S.: High impact strength polypropylene containing carbon nanotubes. Polymer **100**, 259–274 (2016). https://doi.org/10.1016/j.polymer.2016.07.069
46. Murray, A.R., et al.: Factoring-in agglomeration of carbon nanotubes and nanofibers for better prediction of their toxicity versus asbestos. Part. Fibre Toxicol. **9**(1), 10 (2012). https://doi.org/10.1186/1743-8977-9-10
47. Chu, C.-C.; White, K.L.; Liu, P.; Zhang, X.; Sue, H.-J.: Electrical conductivity and thermal stability of polypropylene containing well-dispersed multi-walled carbon nanotubes disentangled with exfoliated nanoplatelets. Carbon **50**(12), 4711–4721 (2012). https://doi.org/10.1016/j.carbon.2012.05.063
48. Bhattacharyya, A.R., et al.: Crystallization and orientation studies in polypropylene/single wall carbon nanotube composite. Polymer **44**(8), 2373–2377 (2003). https://doi.org/10.1016/S0032-3861(03)00073-9
49. Cha, J.; Jun, G.H.; Park, J.K.; Kim, J.C.; Ryu, H.J.; Hong, S.H.: Improvement of modulus, strength and fracture toughness of CNT/Epoxy nanocomposites through the functionalization of carbon nanotubes. Compos. Part B Eng. **129**, 169–179 (2017). https://doi.org/10.1016/j.compositesb.2017.07.070

50. Pan, S.; Feng, J.; Safaei, B.; Qin, Z.; Chu, F.; Hui, D.: A comparative experimental study on damping properties of epoxy nanocomposite beams reinforced with carbon nanotubes and graphene nanoplatelets. Nanotechnol. Rev. **11**(1), 1658–1669 (2022). https://doi.org/10.1515/ntrev-2022-0107
51. Feratoglu, K.; Istif, I.; Gumus, O.Y.: Wear prediction of 3D-printed acrylonitrile butadiene styrene-carbon nanotube nanocomposites at elevated temperatures. J. Polym. Eng. **43**(4), 318–332 (2023). https://doi.org/10.1515/polyeng-2022-0225
52. Rosli, A.A.; Shuib, R.K.; Ishak, K.M.K.; Hamid, Z.A.A.; Abdullah, M.K.; Rusli, A.: Influence of bed temperature on warpage, shrinkage and density of various acrylonitrile butadiene styrene (ABS) parts from fused deposition modelling (FDM). AIP Conf. Proc. **2267**(1), 020072 (2020). https://doi.org/10.1063/5.0015799
53. Younesi, M.; Bahrololoom, M.E.; Ahmadzadeh, M.: Prediction of wear behaviors of nickel free stainless steel–hydroxyapatite biocomposites using artificial neural network. Comput. Mater. Sci. **47**(3), 645–654 (2010). https://doi.org/10.1016/j.commatsci.2009.09.019
54. Greff, K.; Srivastava, R.K.; Koutník, J.; Steunebrink, B.R.; Schmidhuber, J.: LSTM: a search space odyssey. IEEE Trans. Neural Netw. Learn. Syst. **28**(10), 2222–2232 (2017). https://doi.org/10.1109/TNNLS.2016.2582924
55. Lin, T.; Horne, B.G.; Tino, P.; Giles, C.L.: Learning long-term dependencies in NARX recurrent neural networks. IEEE Trans. Neural Netw. **7**(6), 1329–1338 (1996). https://doi.org/10.1109/72.548162
56. D. M. D. Abràmoff, 'Image Processing with ImageJ'.
57. Spoerk, M.; Sapkota, J.; Weingrill, G.; Fischinger, T.; Arbeiter, F.; Holzer, C.: Shrinkage and warpage optimization of expanded-perlite-filled polypropylene composites in extrusion-based additive manufacturing. Macromol. Mater. Eng. **302**(10), 1700143 (2017). https://doi.org/10.1002/mame.201700143
58. Herzberger, J.; Sirrine, J.M.; Williams, C.B.; Long, T.E.: Polymer design for 3D printing elastomers: recent advances in structure, properties, and printing. Prog. Polym. Sci. **97**, 101144 (2019). https://doi.org/10.1016/j.progpolymsci.2019.101144
59. Luo, S.; Zhang, J.: The novel mechanical and recovery behaviors of 3D printed EVA under cyclic tensile loading. Mater. Lett. **360**, 136025 (2024). https://doi.org/10.1016/j.matlet.2024.136025
60. Colak, Ö.U.; Bahlouli, N.; Uzunsoy, D.; Francart, C.: High strain rate behavior of graphene-epoxy nanocomposites. Polym. Test. **81**, 106219 (2020). https://doi.org/10.1016/j.polymertesting.2019.106219
61. J. Vincent, 'Structural Biomaterials: Third Edition', in *Structural Biomaterials*, Princeton University Press, 2012. doi: https://doi.org/10.1515/9781400842780
62. Colak, O.U.: Modeling deformation behavior of polymers with viscoplasticity theory based on overstress. Int. J. Plast. **21**(1), 145–160 (2005). https://doi.org/10.1016/j.ijplas.2004.04.004